NTNU

Norwegian University of
Science and Technology

Radiowave Propagation at Ka-band (20/30 GHz) for Satellite Communication in High-Latitude Regions

Martin Rytír

Master of Science in Electronics
Submission date: June 2009
Supervisor: Odd Gutteberg, IET

Norwegian University of Science and Technology
Department of Electronics and Telecommunications

Problem Description

Increasing demand on capacity and bandwidth makes it desirable to utilize new frequency bands with more available spectrum for satellite communications. Ka-band, already used in some operational satellite systems, is the primary candidate for possible high speed communication links in polar/northern areas, which might become needed as activity from oil exploration and shipping will increase in northern regions.

At present time there is, however, little propagation data collected from these areas and close to none at Ka-band frequencies. Several models exist, but these need to be compared with measurements to ensure validity in high latitude regions.

To increase the knowledge of wave propagation at higher frequencies in Polar/northern areas the tasks are:

- examine the different propagation phenomena and their models

- design, measure and put into operation a measurement station that can be used to collect Ka-band propagation data at NTNU

- compare first measured data with predictions provided by the models

Assignment given: 15. January 2009
Supervisor: Odd Gutteberg, IET

Abstract

Atmospheric impairments are a major obstacle in satellite communications at Ka-band in high latitude regions. This report gives a short summary of the existing models that can be used to model the impairments. Further a simple measurement system based on satellite beacon reception is designed using locally available and off-the-shelf components as well as locally manufactured ones. Performance of the components as well as of the whole system is examined and found to be in agreement with the expected values with overall system figure of merit (G/T) of 21 dB/K. Data from 25 days of measurements are presented and compared with model predictions. The comparison points to possible deficiencies in some of the system components that should be assessed for further use. Most notably low amplitude accuracy of the spectrum analyzer and a low sampling rate of the data acquisition system.

Preface

This thesis is written as the final part of Master of Science degree in Electronics at the Norwegian University of Science and Technology. A study into the atmospheric effects and their models over the whole Norway was done in autumn 2008 and some of the theoretical work is included in this thesis.

I would like to thank professor Odd Gutteberg for his help with many aspects of this thesis, Terje Mathiesen for help with measurement and instrumentation, Tore Landsem and Tore Berg for manufacturing of components, and finally Lars Homb and Svein Andreas Skyttemyr for information about antenna components and feedhorn blueprints.

Martin Rytíř
Trondheim, 25.06.2009

Contents

List of Figures

List of Tables

Abbreviations

Ka-band - frequency band between 17.7 and 21.2 GHz (downlink) and 27-31 GHz (downlink) assigned to satellite communication

RF - Radio Frequency

EIRP - Effective Isotropic Radiated Power

WIMAX - Worldwide Interoperability for Microwave Access – a group of technologies for broadband access

ITU - International Telecommunication Union

CNES - Centre National D'Etudes Spatiales – French National Space Agency

ITU-R - International Telecommunication Union – Radiocommunication Sector

ECMRWF - European Centre for Medium-Range Weather Forecast

LNB - Low Noise Block Downconvertor

IF - Intermediate frequency

RBW - Resolution Bandwidth

RMS - Root Means Square

WLAN - Wireless Local Area network

NOAA - US National Oceanic and Atmospheric Administration

Chapter 1

Introduction

With increasing congestion at lower bands used for satellite communication (L, S, C and Ku-band) as well as due to increasing bandwidth requirements, it is likely that Ka-band will be used by a number of systems in the future. Ka-band uses the frequency between 17.7 and 21.2 GHz for downlink direction and frequency band between 27 and 31 GHz for uplink direction. These bands offer several advantages over the lower bands:

a)Increased Usable Bandwidth and Data-Handling Capacity

Radio-frequency (RF) components operate over a bandwidth related to a percentage of the carrier frequency. For a component with an operating range of 10%, Ka-band offers 2 - 3 GHz of bandwidth against 1.2 - 1.4 GHz at Ku-band or 400 - 600 MHz at C-band.

b)Reduced Size of Components

Size of passive RF components is related to the wavelength used, leading to a reduction of size as higher frequencies are used. On the other hand higher frequency introduces higher losses in the components, partly reducing this advantage.

c)Smaller Satellite Footprints

Using an antenna of same size as at lower frequencies, satellite covers a smaller area while the effective isotropic radiated power (EIRP) in these areas is proportionally increased. This allows utilization of multiple beams making it possible to reuse assigned frequencies.

A main disadvantage of Ka-band frequency systems are increased tropospheric propagation impairments. These are, however, changing rapidly in time making it uneconomical to counter them by simply increasing transmitted power for extended periods. Therefore accurate prediction models are required so that advanced fade mitigation techniques can be introduced.

In Norway and other high-latitude regions, the primary application of Ka-band systems is likely to be high-speed data-transmission to remote locations. As even remote areas of the continental Norway are becoming covered with cellular-based or WIMAX networks, the primary application of these data links is likely to be on ships and platforms located off-shore. Natural resources in the Arctic are likely to become more accessible in the future, triggering increased activity in these high-latitude regions. At the same time with increased use of advanced technology to help harvest these resources, higher transmission speeds are needed, even at these locations. The Iridium Satellite system does offer worldwide data services but at a relatively very slow data rate of 2.4 kbits/s.

The propagation impairments mentioned previously, are highly dependent on the length of the path through the atmosphere. While new satellite systems proposed in highly inclined orbits promise high elevation angles and hence short paths through the atmosphere, it is likely that first systems will use geostationary satellites. Geostationary satellites can cover only areas with latitude lower than 82° and would need to operate on links with very low elevation angles increasing the significance of tropospheric propagation impairments.

Several models presented by the International Telecommunication Union (ITU) as well as other researchers exist for modeling these impairments at Ka-band frequencies, but to date there has been very few measurements that confirm these models at low elevation angles. Previous measurements at low elevation angles were done at Svalbard for Ku-band frequencies [1] and at high frequencies in the South of Norway [2]. It is therefore desirable to perform additional measurements at Ka-band frequencies on low elevation links.

This thesis gives a brief summary of the main propagation phenomena on earth-satellite links and their models, implementing those in MATLAB scripts provided on the accompanying CD as well as using a library made by CNES[3]. ITU-R models are preferred and global data as well as local data inputs are utilized by the models.

A simple measurement system to study the propagation impairments is designed using commercial off-the-shelf components as well as components available at NTNU. The various parts of the system are measured to determine performance and finally the whole system sensitivity is measured.

This simple system is then operated for 3 weeks in May/June 2009 to confirm its function, identify areas which might need change or improvement and try to compare the first measured data with those provided by the models.

Chapter 2

Effects of Atmosphere on Earth-Space Radio Propagation

This chapter discusses the most significant effects for radiowave propagation on earth-space links operating at Ka-band frequencies. Relevant models are presented and explained. Models are chosen according to their applicability on links at hight latitudes and low elevation angles as well as availability of input parameters required by them.

2.1 Clean Air Effects

The gases that the atmosphere consists of are not perfectly transparent to electromagnetic waves, the structure and composition of the atmosphere also varies through an average year. The effects of this on the passing electromagnetic waves are described in this section.

2.1.1 Attenuation by Atmospheric Gases

Atmospheric gases are partially conducting and therefore dielectric. The effect dielectrics have on the propagating electromagnetic wave is described by their complex permittivity ε^* and permeability μ^*. Real part of the complex permittivity and permeability represents the amount of energy stored in the media, while the imaginary part accounts for attenuation (loss) in the media.

Most of the atmospheric gases have non-symmetrical molecules which have a preferred orientation if placed in an electric or magnetic field. This results in resonant character of imaginary parts of complex permittivity or permeability around critical frequencies of the molecule, leading in turn to increased loss at and around these frequencies. Below 70 GHz only atmospheric oxygen and water vapour contribute significantly to the overall attenuation [4]. The respective resonant frequencies are 22.3 GHz for water vapour and about 60GHz for oxygen as can be seen in Figure 2.1.

Several methods for calculating attenuation by atmospheric gases exist. The most accurate method described by ITU-R [5] divides atmosphere into a large number of layers. Specific attenuation is then calculated for each of those layers by summation of contribution from all individual resonance lines of oxygen and water vapour as well as additional factors. Array bending which occurs between the layers is also taken into account when calculating path length.

Total attenuation by atmospheric gases is then given by:

$$A_{gas} = \sum_{n=1}^{k} a_n \gamma_n \quad dB \tag{1}$$

where a_n is the path length through layer n and γ_n is the specific attenuation through the same layer.

Thickness of the layers increases exponentially from 10 cm at ground level to 1 km at 100 km according to:

$$\delta_i = 0.0001 \exp\left(\frac{i-1}{100}\right) \quad km \tag{2}$$

The integration in equation (1) is then performed to at least 30 km. For detailed description see Appendix A1**.**

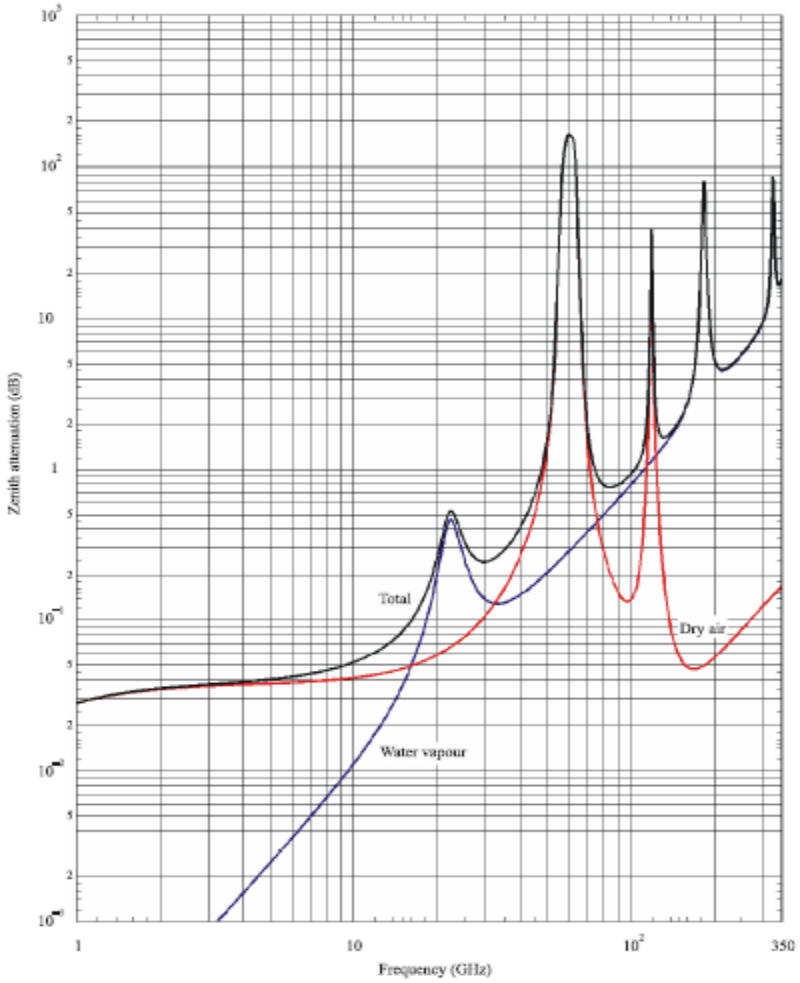

Figure 2.1 Total dry air and water-vapour zenith attenuation from sea level for standard atmosphere. Surface pressure 1013hPa, surface temperature 15 °C, surface water-vapour density: 7.5g/m^3 [5]

While being very accurate, this method needs detailed atmospheric profile of temperature, pressure and water vapour content for reliable calculations of the specific attenuation as well as the path

length. Out of these, water vapour content shows rather large variations during a year, leading to total attenuation increasing in summer and decreasing in winter. Therefore, accurate atmospheric profiles through the whole year are need. This severely limits the practical use of this method.

A simplified method which uses curve-filling of the line-by line calculation is described in the second part of [5]. It approximates the atmosphere by a single layer of oxygen and a single layer of water vapour. Total attenuation is calculated by multiplying path length with the specific absorption of each of the layers. Detailed description is given in Appendix A2. Main advantage of this method is that only surface meteorological data are needed, disadvantage is lower accuracy, especially at low elevation angles, so ITU-R does not recommend using it for elevation angles lower than 5°.

In addition to the frequency dependence shown in Figure 2.1 attenuation by atmospheric gases as well as other attenuation mechanisms described later is highly dependent on elevation angle. Lower elevation angle results in much longer path length through the atmosphere, increasing the attenuation. Figure 2.2 shows dependence on different elevation angles for downlink (20 GHz), and uplink (30 GHz) Ka-band frequencies calculated utilizing the first method and using reference standard atmosphere for high latitudes (>45°) from ITU-R Recommendation P.835-4 [6]. Effect of the water vapour content change through the year is also shown in the figure. The difference between summer and winter values is more prominent at downlink frequencies as these are closer to the water vapour resonance frequency.

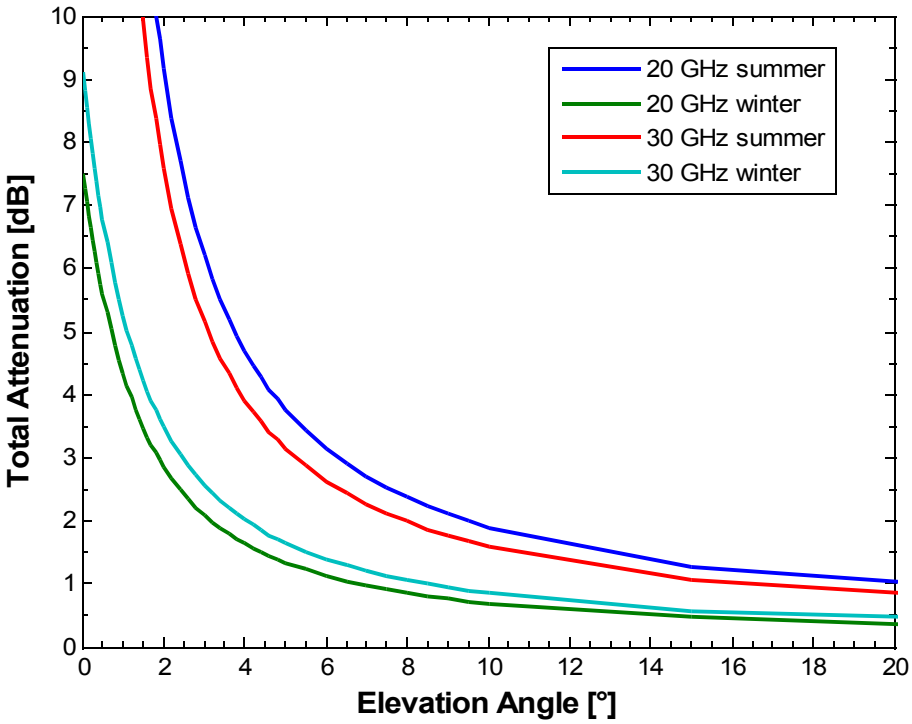

Figure 2.2 Total attenuation by atmospheric gasses with changing elevation angles and different frequencies, using summer and winter reference atmospheres for high latitudes.

2.1.2 Change in Apparent Elevation Angle

With increasing height above surface, atmospheric temperature, pressure and water vapour content on average decrease. Refractive index of the atmosphere – ratio of the speed of radio waves in vacuum to the speed in the medium under consideration, is dependent on all these factors, hence it also decreases with increasing height above surface. Therefore, radio waves between ground station and satellite encounter lower values of refractive index and according to Snell's law bend towards the region with higher refractive index (surface) as shown in Figure 2.3.

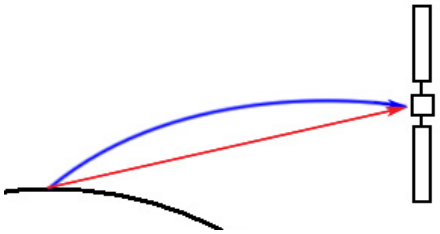

Figure 2.3 Real (red) and apparent (blue) direction to the satellite due to ray bending. Note that in reality most of the bending happens in the lowest parts of the troposphere where refractive index changes most rapidly with height.

This leads to the apparent elevation angle towards the satellite being higher than the real elevation angle. As numerous other effects this one is also highly dependent on the elevation angle. An approximate formula for estimation of the elevation angle correction is given in Appendix A3.

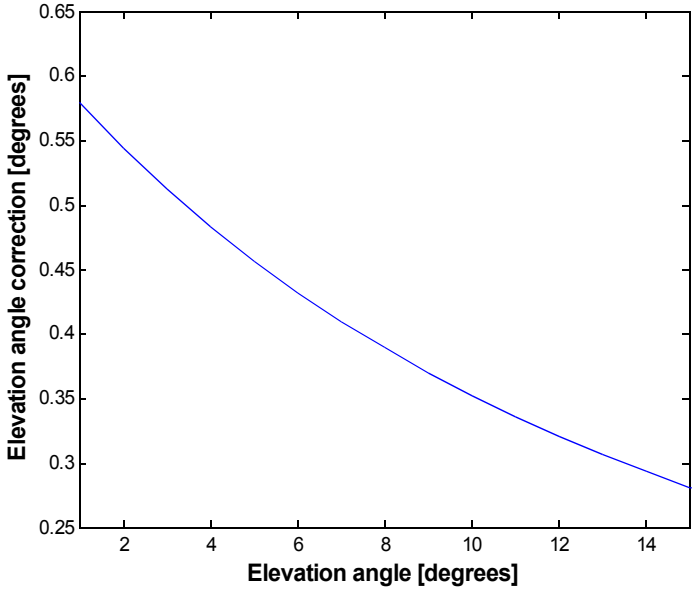

Figure 2.4 Elevation angle correction for different elevation angles and for a station at sea level calculated using the approximation from Appendix A3

In Figure 2.4 results from the approximate method shown in Appendix A3 are plotted. ITU-R also provides average values for this elevation change calculated from measurement [7], which are slightly lower than those plotted in Figure 2.4. Previous measurements for low elevation angles on Svalbard [8] confirmed the ITU-R values and established that the apparent elevation angle changes less than ±0.02° for 95% of time.

Given the small variation it is generally only necessary to correct for the average deviation unless using highly directive antennas and/or at very low elevation angles.

2.1.3 Tropospheric Scintillation

Refractivity decrease described in previous section is, however, not entirely homogeneous with increasing height. High humidity gradients and temperature inversion layers as well as wind cause small scale areas of different refractivity to form in the low levels of atmosphere. The small-scale areas with locally equal refractivity make several propagation paths between the satellite and the ground terminal possible. Multiple secondary waves propagate along these secondary paths and due to a different path length might cause constructive or destructive interference with signal traveling along the main path as well as with each other. These secondary waves are usually smaller in magnitude resulting in signal strength fluctuating around an average level.

Many more small turbulent cells than big ones exist in the atmosphere, with increasing frequency, the shorter wavelength matches the Fresnel lengths of the cells and scintillation becomes more intense. This causes scintillation intensity to increase with frequency. As with other propagation phenomena lower elevation angle also increases scintillation severity due to longer path through the atmosphere. On the other hand large antennas lead to reduction in the scintillation severity due to averaging of the different components over the large area of the antenna.

Several models have been developed to predict these tropospheric scintillations on earth-satellite links. Generally, they can be divided into two groups. First group is represented by Tatarski model [9] and Vasseur model [10] and uses variations in the profile of the atmosphere with height. This profile is represented by structure parameter of the refractive index along the path (C_n). Using these models very good predictions can be made, however, long term measurements of the profile must be available.

Models from the second group require only surface weather data, making worldwide predictions much easier. This group includes ITU-R model [11], van de Kamp model [12], and Karasawa model [kar]. The main meteorological parameter used is the wet component of surface refractivity which can be calculated from water vapour pressure e and surface temperature T using:

$$N_{wet} = 3.732 \text{x} 10^5 \frac{e}{T^2} \qquad (3)$$

Water vapour pressure can again be calculated from relative humidity, see Appendix A4 for details. Reference scintillation standard deviation, σ_{ref} is then in the ITU model calculated using:

$$\sigma_{ref,ITU} = 3.6\,x10^{-3} + 10^{-4}\,x\,N_{wet} \quad dB \tag{4}$$

the predicted scintillation deviation in the ITU model using:

$$\sigma_{ITU} = \sigma_{ref,ITU}\, f^{7/15} \frac{g(x)}{(sin\theta)^{1.2}} \tag{5}$$

And in the Karasawa model using:

$$\sigma_{Karasawa} = 0.0228(0.15 + 5.2\text{x}10^{-3} N_{wet})\, f^{0.45} \frac{\sqrt{G(D_e)}}{(sin\theta)^{1.3}} \quad dB \tag{6}$$

f is frequency in GHz in both models, θ is elevation angle $g(x)$ and $G(D_e)$ are different expressions for antenna averaging factor dependent on frequency, antenna size and path length through the turbulent layer.

Scintillation fade depth exceeded for time percentage p is given by:

$$A_s(p) = a(p)\,\sigma \quad dB \tag{7}$$

where $a(p)$ is given by:

$$a(p) = -0.061(\log_{10} p)^3 + 0.072(\log_{10} p)^2 - 1.71\log_{10} p + 3.0 \tag{8}$$

for both models.

Van de Kamp [12] adds turbulence in clouds into the calculation of reference scintillation deviation:

$$\sigma_{ref,van\ de\ Kamp} = 0.98\,x10^{-4}(N_{wet} + Q) \quad dB \tag{9}$$

$$Q = -39.2 + 56\,\bar{W}_{hc} \tag{9a}$$

where $\bar{W}_{hc}$ is the average water content of heavy clouds at the site.

The first two above mentioned models tend to produce slightly higher prediction than measured [14]-[16]. The model proposed by Van de Kamp and ITU-R models were also compared with measurements at 50 GHz in the south of Norway [2]. While the last method fitted the measurement very well in a few cases, in some cases it also underpredicted them, ITU method overpredicted by some margin in all cases. It should, however, be noted that the method is not recommended to be used over 20 GHz by the ITU. When the frequency exponent in (5) was modified the method nevertheless showed good fit with measurement [2].

All of the mentioned models are not recommended for elevation angles under 4° where scintillation severity increases due to frequency independent low angle effects [17]. ITU recommends another model [11] which calculates deep fading part of scintillation fading at low angles and then interpolates the shallow part of the fading distribution from it.

2.2 Rain and Cloud Effects

In section 2.1.1 water in the form of water vapor was identified as a major attenuation cause. Water in liquid form has similar attenuation affect. The attenuation is, however, made by two components, absorption and scattering. Absorption means that the incident radiowave energy is transformed into mechanical energy which heats the material, if the material has higher temperature than its surroundings, it will then re-radiate the absorbed energy in all directions. Scattering occurs when the radiowave is redirected from its original path without loss of energy to the particle it hit. At low frequencies and for very small size of water drops little energy is scattered out of the path, so attenuation in the propagation direction is mainly due to absorption.

With increasing frequency the raindrop becomes larger compared with the wavelength, leading to increased scattering. Absorption slowly increases as well, leading to overall fast increase in attenuation. Similarly, presence of bigger drops as well as their density contributes to the increase, leading to large increase in attenuation through rain.

As clouds are made of small water droplets or ice. Effects similar to rain of very low intensity occur when electromagnetic waves pass through them. With increased frequency this effect becomes more prominent and needs to be accounted for. Attenuation in snowfall is generally low compared to attenuation caused by rain of the same intensity, except in periods of wet snowfall. During these rare events the attenuation reaches much higher levels than rain of comparable intensity [1]. At present time there are, however no appropriate models for modeling this phenomena.

Another effect rain has on the propagating electromagnetic wave is depolarization. Depolarization in rain is caused by anisotropy of the propagation medium. In light rain, fog or clouds, the raindrops are nearly symmetrical (spherical) and little depolarization occurs. As rain drops get bigger, they are increasingly affected by hydrodynamic forces as they fall. Air resistance on their way to earth causes them to become more flat, while wind tilts them away from vertical. This leads to increased transfer of energy between the vertical and horizontal components of the electromagnetic wave as will be discussed in section 2.2.3.

2.2.1 Attenuation due to Rain

For practical calculations the specific attenuation of an electromagnetic wave propagating through rain with intensity R (mm/h) can be calculated using power law relationship:

$$\gamma_R = kR^{\alpha} \quad dB/km \tag{10}$$

where k and α are dependent on frequency as well as polarization and can be found in ITU-R Recommendation P.838 [18]. Specific attenuation for different rain rates calculated using this equation is shown in Figure 2.5. Note the relatively rapid attenuation increase with increasing rain intensity. When specific attenuation is known, attenuation through rain can be calculated by multiplying (10) by effective path length through rain.

For given location and elevation angle, this parameter can either be found from simultaneous measurement of rain attenuation and rainfall rate (using known specific attenuation) as in [1], or calculated from the rain heigh, which in turn is calculated from mean height of 0° C isotherm since water is in frozen state above this level. The full ITU-R model is outlined in Appendix A5.

Rain intensity for different percentages of time can either be acquired from local measurement or from European Centre for Medium-Range Weather Forecast (ECMRWF) ERA-40 database which is available from ITU-R and represents 40 years of data calculated using a global model and covers whole earth with a resolution of 1.125° in latitude and longitude [19].

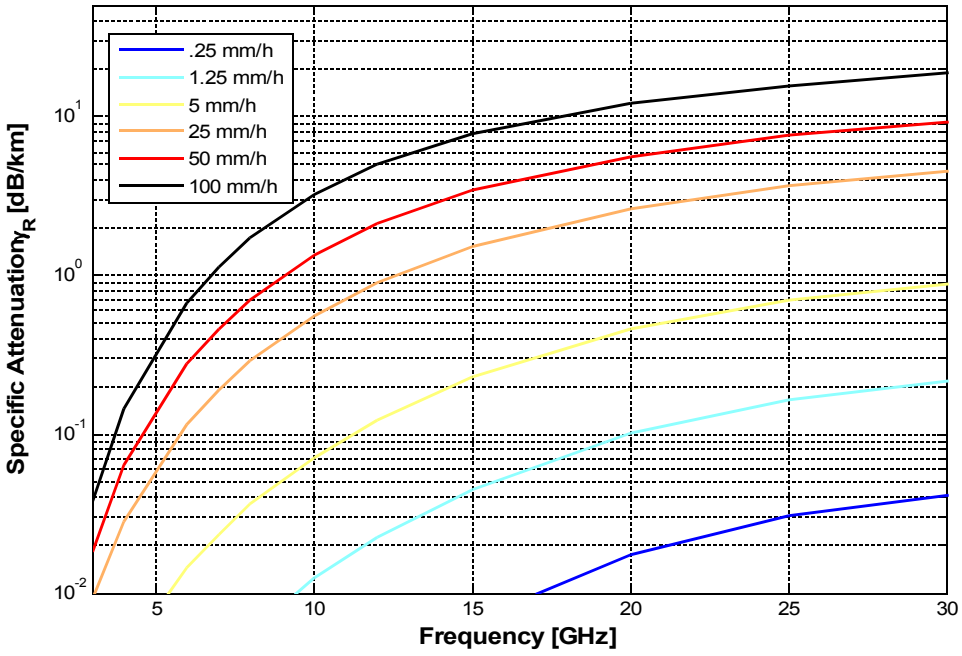

Figure 2.5 Frequency dependence of specific attenuation through rain for different rain rates.

2.2.2 Attenuation due to Clouds and Fog

Clouds and fog consist of small water droplets a few tens of millimetres in size, attenuation of electromagnetic waves propagating through them can therefore be calculated using similar method as for rain. This also implies that the attenuation is of little significance at lower frequencies while it increases with frequency. Specific attenuation within cloud or fog is according to ITU [20] calculated using:

$$\gamma_C = K_1 M \quad dB/km \tag{11}$$

where coefficient K1 is calculated from a mathematical model based on Rayleigh scattering(see [20] for details), and M is liquid water density in the cloud or fog (g/m3).

When total columnar content of liquid water (L (kg/m2)) for a given location is known, total attenuation due to clouds and fog can be calculated using [20]:

$$A_c = \frac{L K_1}{sin\theta} \quad dB \tag{12}$$

where θ is the elevation angle.

2.2.3 Depolarization due to Rain

As mentioned at the beginning of section 2.2, with increasing rain intensity raindrops change their shape into a non-symmetrical one, due to air resistance on their way to ground. Wind then tilts them away from their axis. Different components of the incident electromagnetic wave propagating through rain encounter different impedance, leading them to being attenuated differently. The resulting signal (shown in blue in Figure 2.6) is then tilted from its original axis. Since the receiver still receives only vertical polarization (in this example) part of the signal energy is lost .

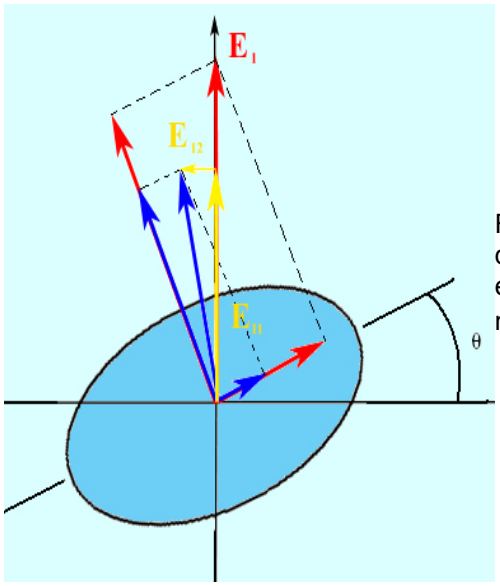

Figure 2.6 Illustration of depolarization through a raindrop due to different attenuation of the major components of an electromagnetic wave. Incident wave is red, resulting wave is blue, new components in horizontal/vertical axes are yellow.

In a similar manner, for a vector with 45° angle (relative to vertical) decomposed into two vectors in horizontal and vertical plane, these two vectors experience different phase shift as they propagate through rain. Leading in turn to the resulting vector tilting with respect to the incident one.

If there are different channels transmitted with vertical and horizontal polarization both these mechanisms lead to unwanted coupling between them. This coupling can be expressed by cross-polarization discrimination (XPD), where XPD is the ratio between the co-polar component and the cross-polar one:

$$XPD = 20\log_{10}\left|\frac{E_{co}}{E_{cross}}\right| \quad dB \tag{13}$$

Dependence of XPD on co-polar attenuation generally takes the form of

$$XPD = U - V\,logA \quad dB \tag{14}$$

where U and V are frequency, elevation angle and tilt angle dependent (angle between the linearly polarized electric field vector with respect to the horizontal). An ITU-R method from [11] for calculating XPD is outlined in Appendix A6.

2.3 System Noise Temperature

Attenuation of the propagating signal is not the only way atmosphere affects the link budget. The additional lossy media along the path emits noise depending on the effective temperature it has. This directly increases the noise temperature of the receiving antenna resulting in a lower G/T ratio.

This additional contribution can be estimated using:[11]

$$\Delta T = T_m(1 - 10^{-A/10}) \tag{15}$$

where:

T_m is the effective temperature of the medium in kelvin and A is attenuation through the medium in dB. For rain, T_m=260° K may be used to obtain upper limit of increase in noise temperature due to rain [11]. The reduction in receiver noise temperature can be calculated as:

$$\Delta(G/T) = 10\log(T_r + \Delta T) - 10\log T_r \quad dB \tag{16}$$

here T_r is receiver noise temperature including antenna noise (without rain).

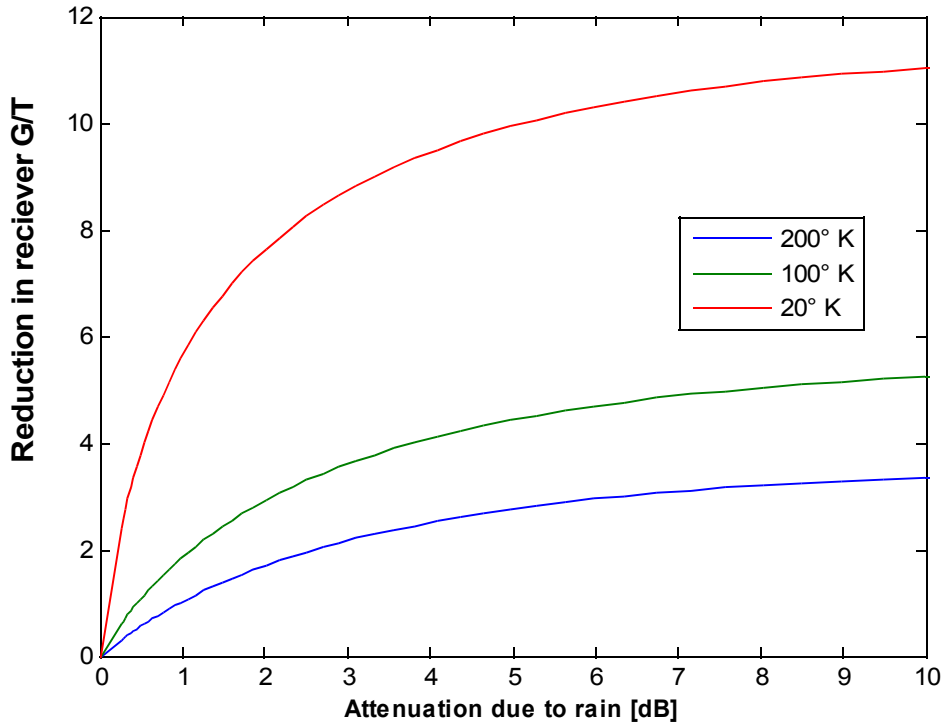

Figure 2.7 Reduction of receiver figure of merit (G/T) due to rain attenuation along the path ,for receivers with T_r = 20, 100 and 200°K.

The reduction is much higher for receivers with low system noise temperatures as shown in Figure 2.7. For example for a receiver with a 20° K noise temperature the reduction in signal-to-noise ratio when attenuation due to rain on the path is 4 dB will be 4 dB (attenuation) + 9.5 dB(noise) = 13.5 dB in total.

Chapter 3

Measurement setup

Using commercially available components as well as antennas already available at NTNU a simple measurement system was designed and put into operation. The system was designed to measure satellite beacon signals transmitted by satellites already in orbit. These beacons are mostly continuous wave transmitters operating at fixed power and have many purposes, one of which may be estimation of attenuation along the path. Most of the transmitted energy is contained within a very narrow bandwidth around the central frequency, provided the carrier is not modulated. Receivers can therefore be designed as narrowband. Since the noise in the receiver is proportional to the bandwidth it will be quite low, permitting either a large dynamic range to be achieved or a very small antenna to be used.

In the following chapter the various components of the measurement system are described, their parameters confirmed by measurement and a final link budget is presented. It was, however not possible to measure radiation pattern of the whole antenna due to size and operating frequency.

3.1 Satellite

Long-term measurements are needed to investigate the propagation phenomena. Therefore geostationary satellites are best suited for attenuation measurements, due to their relatively fixed position and hence constant elevation and distance allowing direct observation of the attenuation phenomena. In high latitude regions, the low elevation towards geostationary satellites also makes propagation phenomena more prominent. Geostationary satellites are, however, not above the visible horizon over approximately 82° latitude provided the satellite is at same longitude as the receiver.

An option is to use a beacon transmitted by the Advanced Relay and Technology Mission (ARTEMIS) satellite. This satellite launched in 2001 did not initially reach the planned orbit and an onboard ion propulsion system originally designed only for inclination control had to be used to bring the satellite into geostationary orbit. This in turn caused low amount of fuel for inclination control and at present time its inclination is gradually increasing. In January 2009 it was about 7° [21]. This allows the satellite to be visible also in areas located above 82° of latitude. As a disadvantage the distance as well as the elevation angle towards the satellite changes, reducing the amount of comparable data and requiring a tracking antenna at the receiver. For this reason it was not chosen as the primary signal source but the receiver operating frequency was chosen to make reception of ARTEMIS signal possible pending simple modifications.

Instead a commercial telecommunication satellite was chosen. Compared with the large number of satellites operating in Ku-band and lower, the number of Ka-band satellites is relatively small. The satellites beacons available in Trondheim and Southern Norway are listed in Table 1, apart from those listed Astra 1L and Astra 4A should also have Ka-band transponders but it is not known whether they are sending any beacons at these frequencies. Out of those listed Hot Bird 6 was chosen due to the operating frequency being closer to ARTEMIS than Eutelsat W3A, allowing the use of same LNB. The 3 military communication satellites were not considered due to possible difficulties in obtaining satellite status information.

Satellite Name / Position	Owner / Mission	Beacon Frequency in MHz / Polarization	
Syracuse 3B / 5° W	France / Military Communication	20250	[22]
Eutelsat W3A / 7° E	Eutelsat / Communication	**21404 / H**	[22]
Hot Bird 6 / 13° E	Eutelsat / Communication	**19701 / H**	[22]
Sicral 1B* / 13.3° E	Italy / Military Communication	20250	[22]
Sicral 1A / 16° E	Italy / Military Communication	20250	[22]
ARTEMIS / 21.5° E (inclined)	ESA / Communication Research	**20110 / V**	[21]

*Launched 20. April 2009

Table 1 Ka-band satellite beacons available in Trondheim

The Hot Bird 6 communication satellite operated by Eutelsat was launched in August 2002 and has expected lifetime of over 12 years. It carries 28 Ku-band and 4 Ka-band transponders. The Ka-band transponders are used for a satellite Internet service called Too Way. It currently has a maximum customer downlink speed of 3.6 Mbps and over 1 Mbps on uplink. System speeds are 72 Mbps maximum on downlink and 2.4 Mbps on uplink. User equipment sold with the service uses a dual reflector antenna with a primary reflector diameter of 68 cm and achieves a typical G/T ratio of 17 dB/K [24]. The system uses uplink power control and adaptive coding and modulation (ACM) to mitigate rain fade.

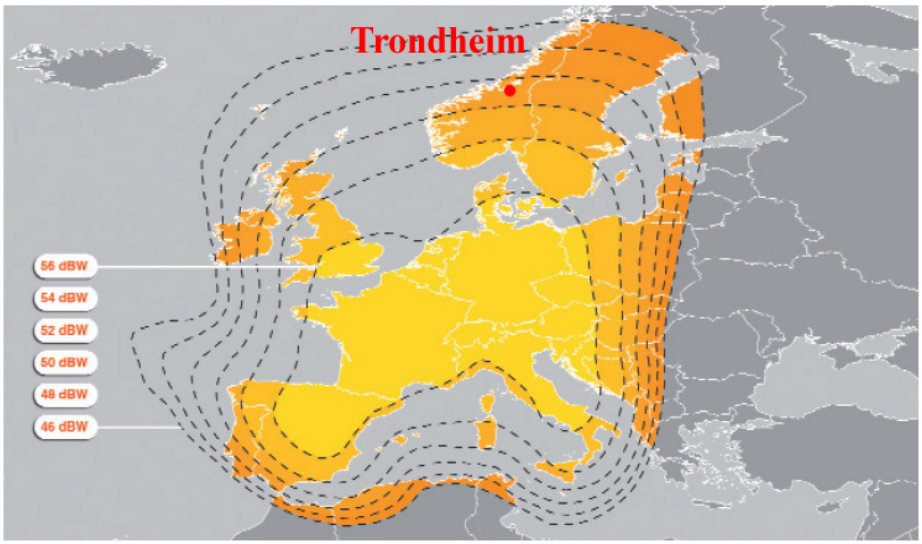

Figure 3.1 Hot Bird 6 Downlink Coverage [23] with marked location of Trondheim

Figure 3.1 shows downlink coverage map for the Hot Bird 6 Ka-band transponders. Information about beacon EIRP is, however, not publicly available.

From the current measurement location at approximately 63.418° N, 10.400° E, 50 meters above sea level the Hot Bird 6 satellite is located at azimuth of 177° and has an elevation of 18.354° as calculated by AGI Satellite Toolkit Software taking into account refraction along the path. The beacon should have horizontal polarization tilted 3.5° in relation to the equator, due to different longtitude of the satellite and the earth station this tilt should be reduced to about 2°.

3.2 Receiver

This section describes the various outdoor and indoor parts of the receiver. Most of the components were measured separately before assembly to confirm their parameters, results of these measurements are also presented. Final link budget for the whole system is calculated to asses performance.

As mentioned at the beginning of this chapter the receiver was designed to use commercially available components as well as components already at NTNU or those that could easily be manufactured. The author is aware that there are several areas where the receiver and data acquisition can be further improved, those are discussed in Chapter 5.

3.2.1 Antenna and Feedhorn Assembly (Outdoor part)

Gregorian offset antenna designed for operation in Ku-band and manufactured by FIBO was used in the system. The dual reflector antenna has a main reflector of 99 x 90 cm and originally had a maximum gain of 40 dBi at a frequency of 11.7 GHz, see Appendix A7 for specifications. For operation at Ka-band a new feedhorn was installed as well as associated waveguide convertors and a Ka-band LNB. The final configuration is shown in Figure 3.2.

Blueprints for a Ka-band corrugated conical feedhorn that was used on an antenna of same type previously were provided by Svein A. Skyttemyr and are included in Appendix A8. The horn was manufactured from aluminum at NTNU. Due to very small dimensions and high precision needed it was manufactured from several rings assembled together. The horn uses a non-standard waveguide diameter in order to be usable over the whole Ka-band spectrum used in satellite communication. Two options were therefore available in order to connect it to the LNB. Either direct convector from non-standard circular waveguide to a rectangular one used on the LNB input or a two step solution. In the end the two step solution was chosen due to cost and time constrains. A simple quarter-wave convertor between different diameters of the circular waveguide was designed and manufactured locally and a standard circular-waveguide convertor was purchased from Custom Microwave. See Appendix A9 for details on the design of the circular-circular convertor.

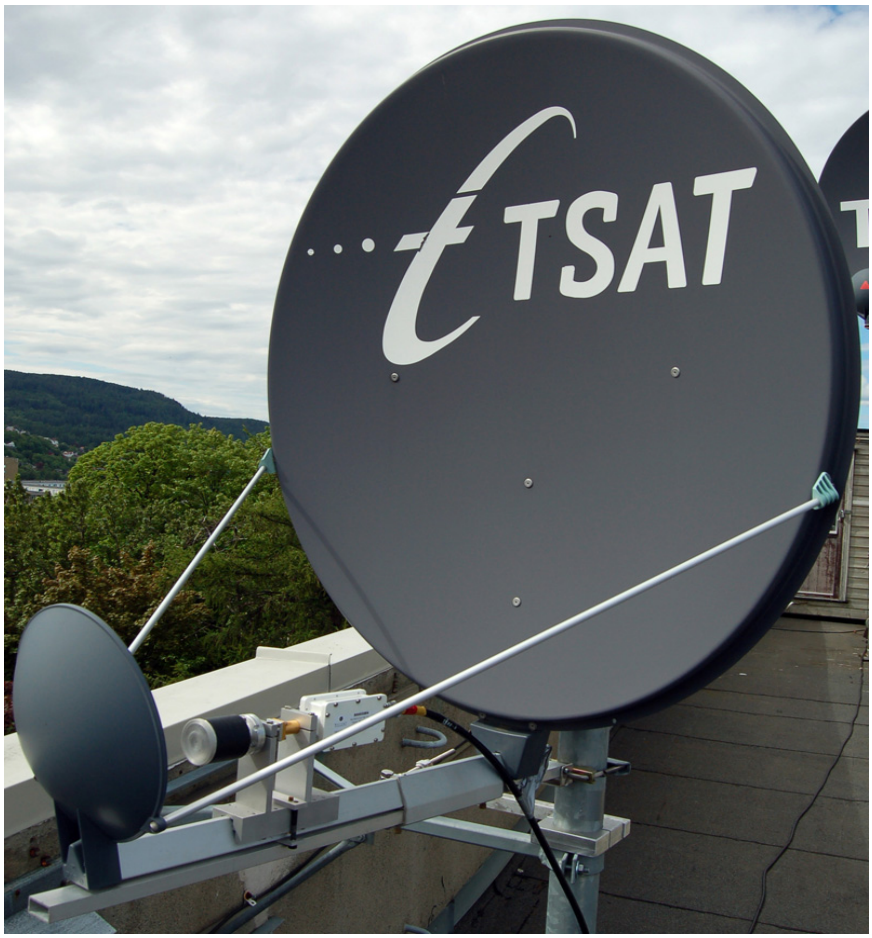

Figure 3.2 Receiver antenna with mounted feed and LNB.

Low Noise Block Downconvertor from Norsat International - 9000XBN was used for conversion to IF and reduction of system noise temperature. It converts the 19.2 – 20.2 GHz band down to 950 -1950 MHz IF. This LNB requires external reference frequency generator that its local oscillator is phase locked to. The advantage of this arrangement is a better frequency stability compared with LNBs that use LO only. This extra stability is required so that a narrow-band receiver can be used. For LNB specifications see appendix 8. To avoid water intrusion into the horn and waveguide a plastic cap was added to the horn and all connections were sealed with silicone.

Figure 3.3. shows the feed assembly with all the components. The custom mount in the picture was designed to allow for easy adjustment of the horn position in order to optimize it relative to the focal point of the secondary reflector of the antenna. The focal point should be located 92 mm above the surface of the boom connecting the reflectors and 200 mm from the centre of the secondary reflector.

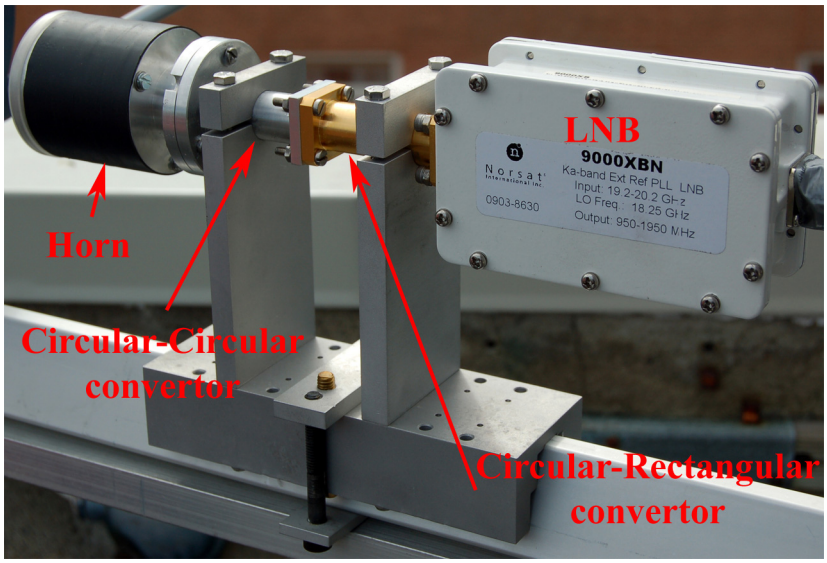

Figure 3.3 Detail of the feed with component description

3.2.1.1 Feed Assembly Measurement

As the feedhorn and one of the adapters were manufactured by the institute workshop it was necessary to confirm their functionality as well as characteristics. Effect of the plastic cap, which protects the feedhorn from water and foreign objects, on the radiation pattern also had to be assessed.

Measurement setup

Measuring Equipment and Measured Devices

- Anechoic chamber
- Antenna tower with steerable measurement plate
- 2 Flann Microwave Standard Gain Horns, type 20240
- Newport MM4005 Motion Controller
- Hewlett Packard HP 83017A Broadband Microwave Amplifier
- Agilent E8364B Network Analyzer, 10MHz – 50 GHz
- Ka-band feedhorn, own designed circular waveguide step converter, Custom Microwave CR42S-4547S Circular-Rectangular Waveguide adapter, 2 Suhner Series 3100 WR-42 Waveguide-SMA adapters 18-26.5 GHz

The feed assembly consisting of the conical horn, circular waveguide step converter and circular-rectangular waveguide adapter together with the mounting was placed on a wooden plate with same upper dimensions as boom of the Fibo antenna. This plate was then mounted on a rotating plate inside the anechoic chamber so that the axis of the feedhorn was in same height as the axis of the transmitting horn. The measured antenna was connected to Port 1 of the Network analyzer, while signals from Port 2 were first amplified by the broadband amplifier and then transmitted by the standard gain horn. During measurement PC controls the rotation of the plate using the motion controller, records the position and retrieves and saves measured S12. See Figure 3.3 for reference.

Measurement setup

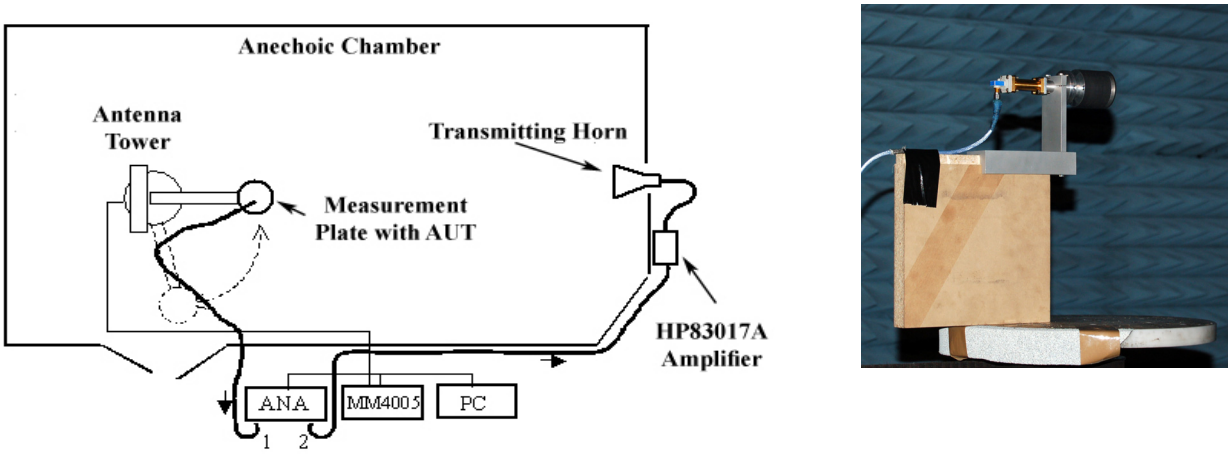

Figure 3.4 Measurement setup and detail of the rotating plate with the feed assembly

The measured radiation pattern was then normalized to the maximum value. To determine maximum gain of the feedhorn a second standard gain horn was measured at exactly same location as the feedhorn. The difference between the measured gain was then subtracted from known gain of the standard gain horn to determine gain of the feedhorn. It should be noted that the gain measured by this procedure includes losses in both the circular waveguide step converter and in the circular-rectangular waveguide adapter.

Measurement Results

Early measurements shown in Figure 3.5 display a significant difference between the radiation pattern with and without the plastic cap protecting the horn from water and foreign objects intrusion. This original cap (Cap 1) made out of acrylate polymer had average thickness of about 1.7 mm. To minimize this effect a new much thinner cap (Cap 2) was manufactured from the same material having a thickness of about 0.5 mm. As Figure 3.5 shows the new cap has much smaller effect on the radiation pattern of the horn.

Radiation pattern in both E and H plane was then measured with this new cap on. Results in Figure 3.6 show similar beamwidth in both planes as well as the absence of significant sidelobes. It should, however, be noted that the sidelobe level is near the end of the available dynamic range of the measurement setup at this frequency, as witnessed by their noisy character. The measurement frequency is also at the upper end of the anechoic chamber specification and results show slight asymmetry of the radiation pattern caused by asymmetry of the chamber (access door and access path). This was confirmed by subsequent measurements of the feedhorn rotated 180°.

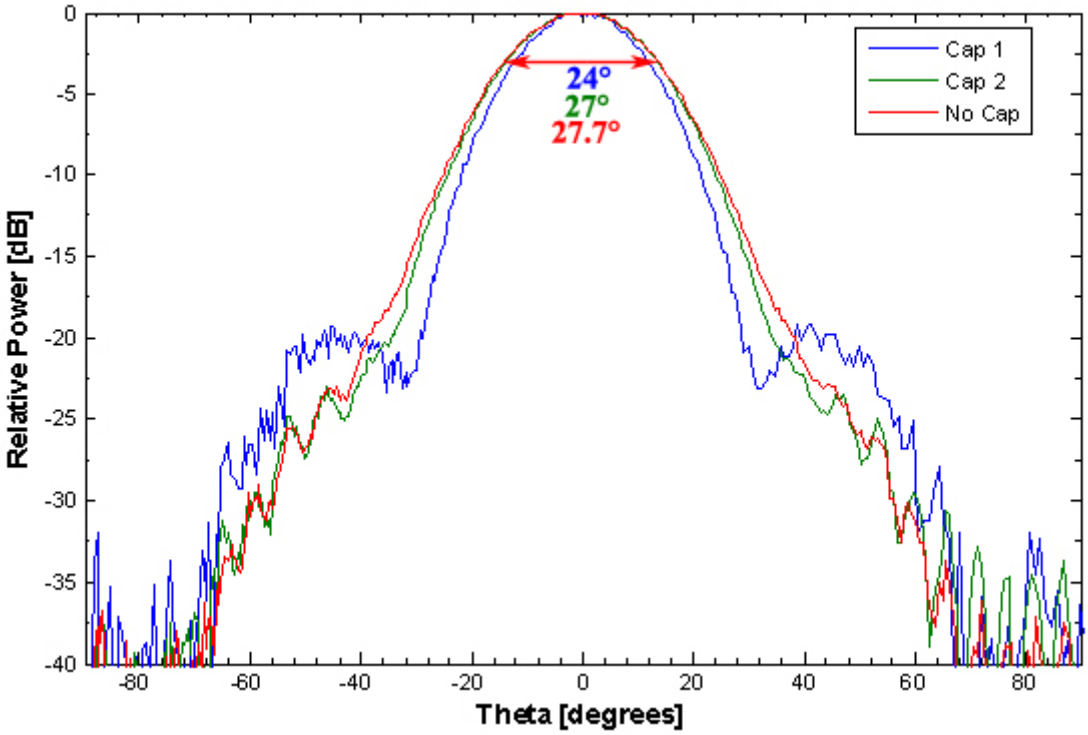

Figure 3.5 E-plane radiation pattern of the feedhorn assembly at 19.701 GHz, with 2 different caps as well as without cap. 3 dB beamwidths are marked in the figure.

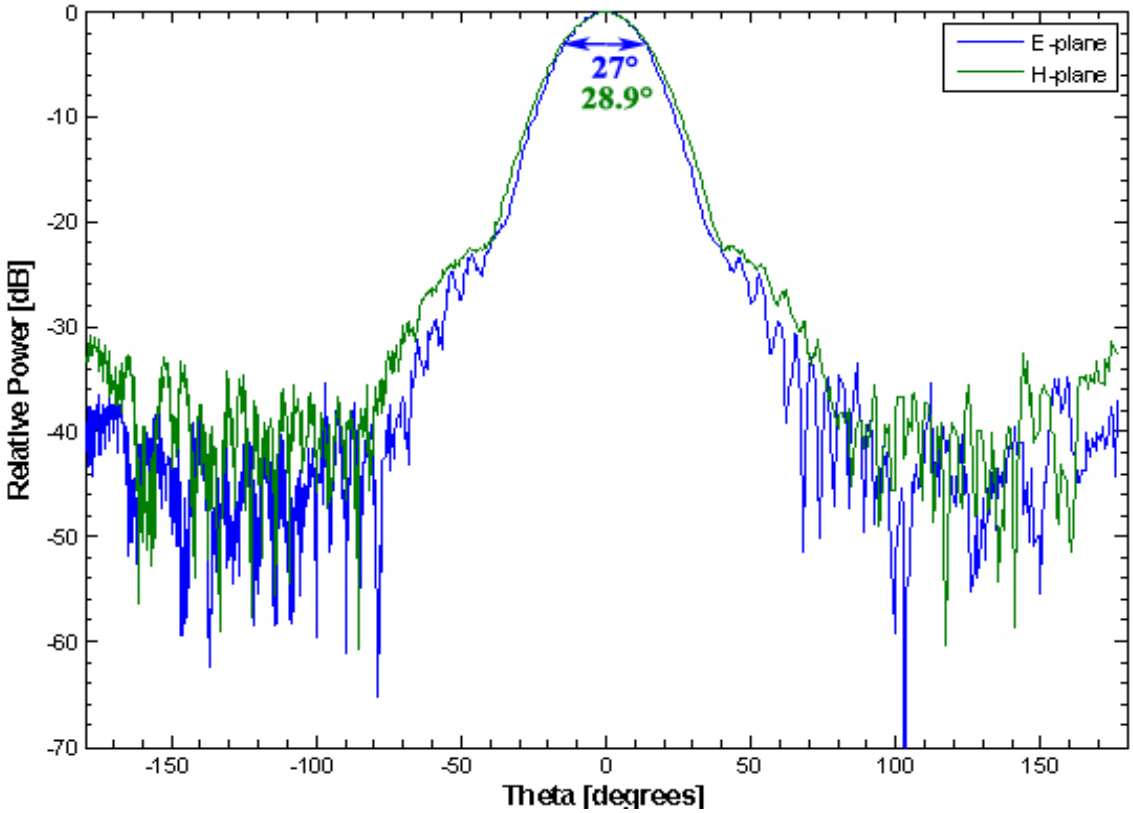

Figure 3.6 Radiation pattern of the feedhorn assembly in both planes at 19.701 GHz. 3 dB beamwidths are marked in the figure.

Measurement setup

In Table 2, the measured S12 for both horns and the calculation of feedhorn maximum gain is listed. For comparison characteristics of a corrugated conical horn with aperture radius of 24.5 mm and axial horn length of 58 mm were calculated in PCAAD 5.0 program. Results were a maximum directivity of 16.9 dBi and -3 dB beamwidths of 25° and 24° in E- and H-planes.

Measured S12 for Feedhorn [dB]	-31.7
Measured S12 for Standard Gain Horn [dB]	-28.9
Difference [dB]	-2.8
Standard Gain Horn gain at 19.7 GHz [dBi]	19 (±0.25)
Feedhorn Gain at 19.7 GH[dBi]	**16.2**

Table 2 Feedhorn maximum gain and its calculation

3.2.1.2 Low Noise Block Downconvertor (LNB) Measurement

To confirm the specifications provided by the manufacturer the Noise Figure and Gain of the LNBs was measured over their whole frequency range.

Measurement setup

Measuring Equipment and Measured Devices

- Hewlett Packard FSQ-40 Signal Analyzer with FS-K30 Application Firmware for Noise Figure and Gain Measurements
- Hewlett Packard 346C_K01 Broadband Noise Source 1-50GHz
- Suhner Series 3100 WR-42 Waveguide-SMA adapter 18-26.5 GHz
- 2 Norsat 9000XB Low Noise Block Downconvertors (LNBs) 19.2-20.2 GHz
- Hewlett Packard 33120A arbitrary waveform generator for 10 MHz reference
- TTi E302 Power Supply
- Anritsu K241C Power Splitter, Bias tee for power supply connection
- Suhner 20 dB and 10dB attenuators, N-SMA adapter, SMA male-male adapter, 2 SMA-Bayonet adapters Suhner Sucoflex 100 cables
- Hewlett Packard 8510C Network Analyzer
- Hewlett Packard 8753E Network Analyzer 30kHz – 6GHz

Excess Noise Ratio (ENR) values of the Noise Source were manually entered into the Signal Analyzer and calibration was performed using just the Noise Source connected to the input of the Analyzer as shown in Figure 3.7. Since the LNB is downconverting the signal in frequency, FSQ-40 needs to be setup for this prior to calibration. In this mode the Analyzer is calibrated for the IF frequencies (950-1950 MHz) on the output of the LNB, but uses correct 19.2-20.2 GHz ENR values during the measurement itself.

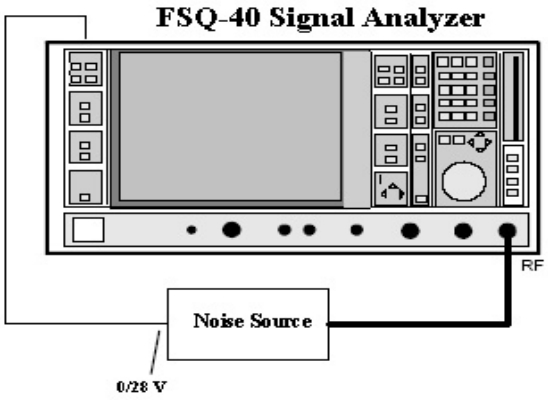

Figure 3.7 Calibration setup for LNB measurement

Measurement setup itself is shown in Figure 3.8. SMA -WR 42 waveguide adapter is needed to connect the Noise Source to the LNB itself. This introduces added loss that at this position can severely affect the measured noise figure. Therefore the adapter loss at 19.2-20.2GHz had to be measured using the HP8510C Network Analyzer prior to starting the measurement. The measured values were then entered into the FSQ-40 for build-in compensation. In a similar manner the Bias Tee, Splitter and Attenuators introduce added loss on the output of the LNB. While these do not have significant effect at the resulting Noise Figure, they do affect the Gain measurement. Loss of all these components connected at the output over the IF frequency band was measured using HP8753 Network Analyzer and the values were entered into the FSQ-40 for compensation. The attenuators between the splitter and the FSQ-40 are added to keep overall gain in 20-30 dB range, which is recommended for best precision in the FSK-30 software manual. The attenuation between the splitter and the reference generator server to reduce any reflections from the generator output.

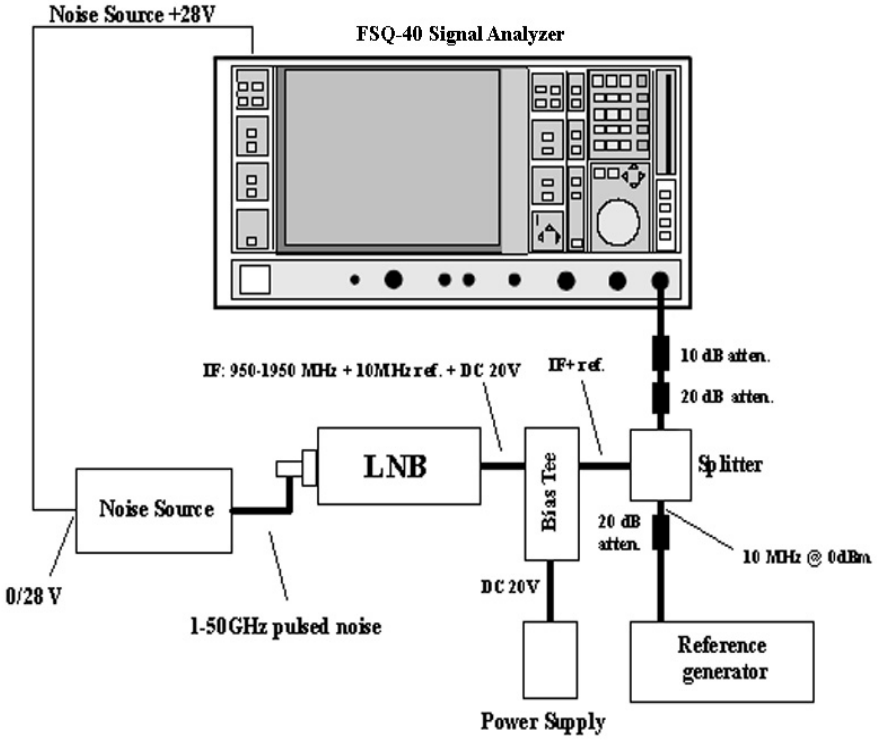

Figure 3.8 LNB measurement setup

Measurement Results

Both LNBs were kept operating for 15 minutes prior to measurement to reach stable operating temperature. Gain results were nearly identical compared with cold values, but noise figure was significantly affected. Measurement results shown in Figures 3.9 and 3.10 indicate a gain higher than the 56 dB listed in specification while noise figure at 19.7 GHz is about the same as in specification. Based on these results, LNB with serial number ending with 012 was chosen to be used.

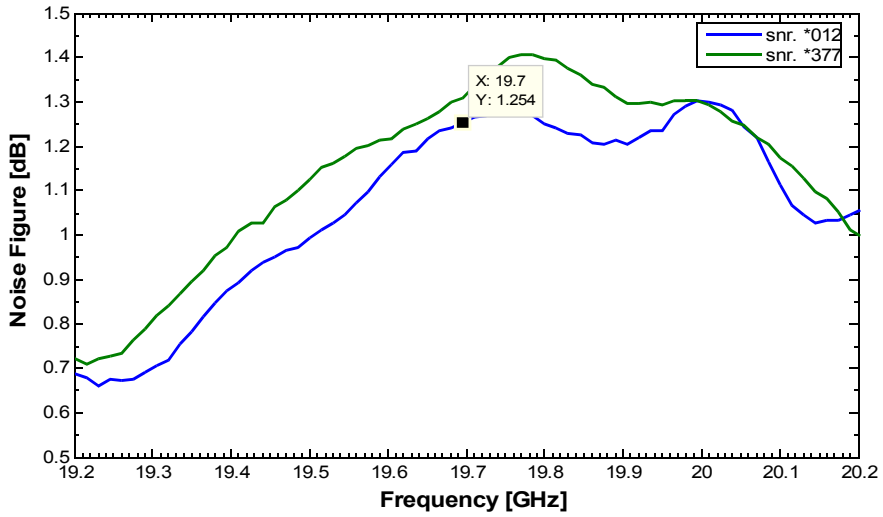

Figure 3.9 Measured noise figure

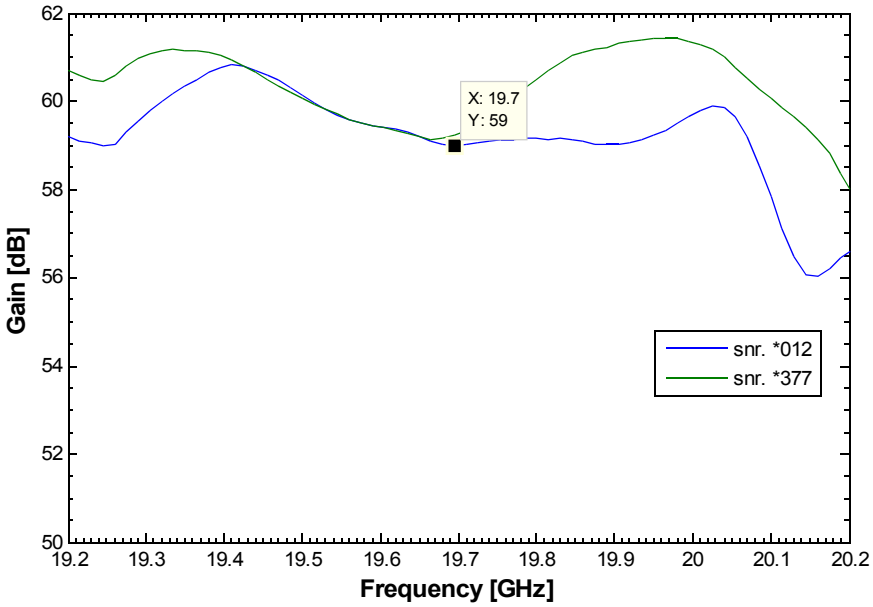

Figure 3.10 Measured gain

3.2.2 Receiver indoor part and data acquisition

The IF signal from the LNB goes through a coaxial cable to the indoor part of the receiver showed in Figure 3.11. First it passes through a bias tee which is used for separating the DC voltage of the power supply from the rest. Next is an Anritsu K241C Power Splitter which is used to connect the reference generator. To suppress reflections on the IF frequency a 10 dB attenuator is added between the splitter and the reference generator. The IF signal is then led to an Agilent MS2721A spectrum analyzer.

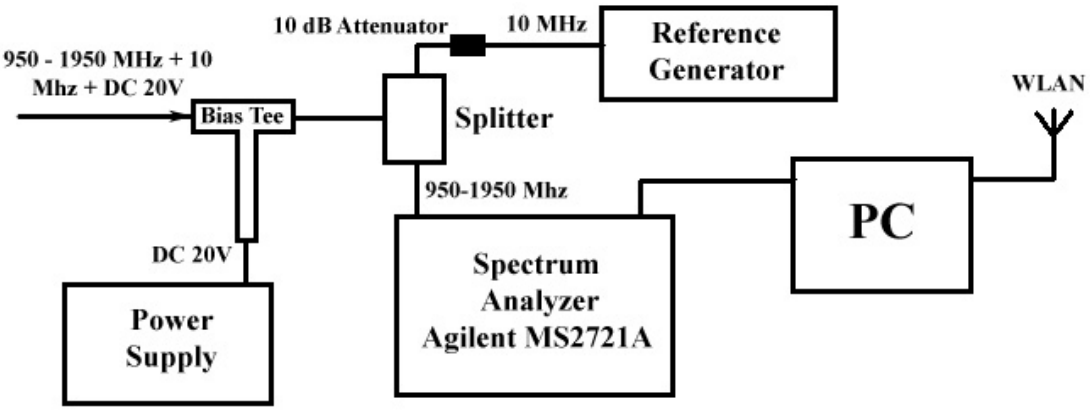

Figure 3.11 Schematic layout of the indoor part of the receiver

The spectrum analyzer is set to a RBW (Resolution Bandwidth) of 300 Hz and RMS detection. This means that it measures the power through a 300Hz filter using a true RMS power detector. At the same time noise power in a 10 kHz band immediately above the beacon frequency is measured using the build-in channel power measurement. Disadvantage of using the spectrum analyzer instead of a power meter is lower accuracy of measurement. Absolute amplitude accuracy is only ±1.5 dB according to the spectrum analyzer specifications [25], relative accuracy is, however, not listed. Advantage over a power meter is no need for narrow band external filters as well as the ability to check the frequency spectra received.

The spectrum analyzer was connected to a PC through a network cable. National Instruments Labview software was used to collect data from the analyzer. To obtain as much data as possible the program was set to record data as fast as possible which resulted in a new value saved approximately every 4 seconds but with some variation. Since each data entry includes a day/hour/minute/second timestamp it is no problem to identify the time elapsed. The PC was connected to the Internet using WLAN University network for the purpose of time synchronization as well as remote access.

3.2.3 Receiver G/T

Figure of merit (G/T) is the main parameter used to determine the sensitivity of a receiver. In this section the best/worst expected values are calculated and compared with measured value.

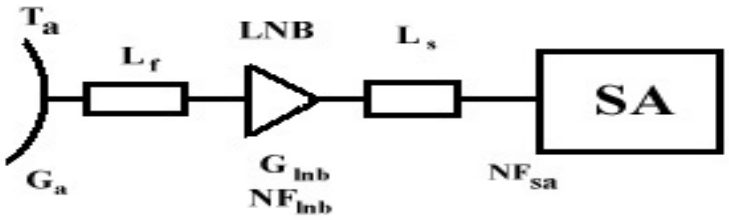

Figure 3.12 Simplified receiver overview

In Figure 3.12 a simplified block overview is shown. The parameters shown are:

T_a , G_a - noise temperature and gain of the antenna
L_f - loss in the waveguide convertors and due to impedance mismatch on LNB input
G_{lnb}, N_{lnb} - gain and noise figure of the LNB
L_s - loss in the IF cable, the bias tee, splitter and cable leading to SA
NF_{sa} - is the noise figure of the spectrum analyzer

Antenna gain of an antenna with parabolic primary reflector can be calculated using:

$$G = eff\,(\frac{\pi D}{\lambda})^2 \qquad (17)$$

here *eff* is aperture efficiency and *D* is aperture diameter in meters.

As listed in Appendix A7 gain of the antenna with the original feed was 40 dBi at 11.7 GHz, antenna efficiency based on 90 cm diameter was 82%. Therefore we can assume 82% to be maximum theoretical limit for the antenna with our feed, 50 % is used as a worst case lower limit. Using the above formula, maximum gain of the antenna at 19.701 GHz lays between 42.36 and 44.51 dBi.

Antenna noise temperature as listed in the specification in Appendix A7 is 23.1 K for elevation angles down to 20°. At 19.7 GHz and for elevation angle of 18.3 GHz it is assumed to be 50° K based on [26].

Losses in the feed are difficult to determine accurately without the ability to measure them. As a minimal value they were assumed to be negligible and as a maximum 0.76 dB was used. This value comes from maximum input VSWR of the LNB listed in appendix X to be 2.2:1 (0.66 dB loss) and 0.1 dB added for losses in the two convertors.

Gain of the LNB was measured to be 59 dB at 19.701 GHz, noise figure 1.254 dB. Loss in the IF cable was measured to be 5.2 dB and loss in bias tee, splitter and final cable to be 6.4 dB, giving 11.6 dB in total. Noise figure of the spectrum analyzer is 14 dB according to specification [25].

Noise temperature referenced at the input of the LNB can then be calculated using:

$$T = \frac{T_a + T_f}{L_f} + T_{lnb} + \frac{T_s}{G_{lnb}} + \frac{T_{sa} L_s}{G_{lnb}} \tag{18}$$

Noise temperature in this equation is calculated from noise figure using:

$$T_e = (NF - 1)\,290 \tag{19}$$

for a lossy line at room temperature NF = L.

The two last terms in equation (18) are equal to about 0.1 K and can therefore be ignored in the calculation.

Aperture efficiency and feed loss are two parameters that could not be determined by measurement, therefore Table 3 presents min., middle and max. values of these two parameters and gives estimated G/T range based on them.

	Min	Middle	Max
Antenna diameter [m]	0.9	0.9	0.9
Aperture efficiency [%]	50	66	82
Antenna Gain [dBi]	42.36	43.57	44.51
Feed loss [dB]	0.76	0.38	0
Total gain [dB]	**41.6**	**43.19**	**44.51**
Antenna Noise Temperature [K]	50	50	50
Feed noise temperature [K]	55.5	26.5	0
LNB noise temperature [K]	97	97	97
Total noise temperature (18) [K]	**185.5**	**167**	**147**
G/T [dB/K]	**18.9**	**21**	**22.8**

Table 3 G/T calculation summary

3.2.3.1 Receiver G/T measurement

To confirm the calculations the figure of merit of the receiver was measured using the fully assembled system.

Theoretical Background

Y-factor measurement was used to determine the G/T. The principle is to measure the increase in noise power measured by the receiver when the antenna is first pointed at a region of cold sky and them at a source of known radiation flux. Sun, Moon or radiostars can be used as this source. Due to relatively low expected G/T the sun was used during this measurement.

Y-factor is then given as:

$$Y = \frac{P_{sun}}{P_{cold\ sky}} \tag{20}$$

G/T can be calculated using [27]:

$$\frac{G}{T} = \frac{(Y-1)8\pi k L}{F \lambda^2} \tag{21}$$

where:

k is Boltzmann's constant – 1.38 e-23 [j/K]

F is solar flux density at the operating frequency [W/m^2/Hz]

λ is operating wavelength

L is beamsize correction factor given by:

$$L = 1 + 0.38\,(W_s / W_a)^2 \tag{22}$$

W_s is radiating diameter of the sun at the operating frequency

W_a is antenna -3dB beamwidth at operating frequency

Calculations and Results

The measurement was performed on 22.05.2009, sky was clear except for a few white clouds, which were not located near the sun. To avoid problems with aiming of the antenna the measurement was performed at 11:06:36 UTC, the exact time that sun azimuth equalled Hot Bird 6

satellite azimuth at the location. This way it was only necessary to adjust elevation to point the antenna towards the sun. Sun elevation at that moment was 47° which is far enough from the satellite at 18.4° to neglect possible interference.

Solar flux density data was obtained from US National Oceanic and Atmospheric Administration (NOAA), Space Weather Prediction Center. Nearest station NOAA operates is in San Vito, Italy (40.6° N, 17.7° E). Values provided are listed below:

:Product: Solar Radio Data 45day_rad.txt

:Issued: 2252 UTC 25 May 2009

#

Prepared by the U.S. Dept. of Commerce, NOAA, Space Weather Prediction Center

Please send comments and suggestions to SWPC.Webmaster@noaa.gov

Units: 10^-22 W/m^2/Hz

Missing Data: -1

#

Daily local noon solar radio flux values - Updated once an hour

#

Freq	Learmonth	San Vito	Sag Hill	Penticton	Penticton	Palehua	Penticton
MHZ	0500 UTC	1200 UTC	1700 UTC	1700 UTC	2000 UTC	2300 UTC	2300 UTC
2009 May 22							
245	12	13	12	-1	-1	11	-1
410	28	-1	27	-1	-1	29	-1
610	35	-1	38	-1	-1	37	-1
1415	58	57	60	-1	-1	59	-1
2695	73	77	81	-1	-1	77	-1
2800	-1	-1	-1	72	-1	-1	-1
4995	121	115	120	-1	-1	120	-1
8800	219	228	223	-1	-1	217	-1
15400	509	506	530	-1	-1	514	-1

The value at 19701MHz was obtained by plotting the measured data and interpolating it with a cubic spline function giving a value of 677 e-22 [W/m^2/Hz]. NOAA values were measured at 12 UTC with sun elevation angle of 64.4°, so the actual value in Trondheim might be slightly lower due to longer path through the atmosphere.

For beamsize correction factor calculation, W_s was estimated to be 0.5 degrees [27]. W_a was approximated by calculating the theoretical beamwidth at 14.25 GHz and 19.7 using $W_a = 72 (\lambda/d)$. Difference between resulting 1.68° and 1.22° degrees was subtracted from measured beamwidth of 1.5° at 14.25 GHz (Appendix A7) giving W_a of 1.04°.

Measured		**Theoretical**			
Y [dB]	8	Total gain [dB]	41.6	43.19	44.51
L	1.09	Total noise temperature [K]	185.5	167	147
F [10^-22 W/m2/Hz]	677				
G/T [dB]	**21.1**	**G/T [dB]**	**18.9**	**21**	**22.8**

Table 4 Measured G/T and comparison with theoretical values

Measured G/T was 21.1 dB/K which lays within the limits given by theoretical calculations. As the Y-factor was read out as a difference between noise levels on a spectrum analyzer it remains accurate only within about ± 1.5 dB leading to a G/T uncertainty of ± 1.7 dB.

3.3 Link budget

Received signal to noise ratio is calculated using:

$$\frac{C}{N_0} = EIRP_{sat}\left(\frac{\lambda}{4\pi R}\right)^2 \frac{1}{k}\frac{G}{T} \qquad (23)$$

here R is the distance towards the satellite and k is Boltzmann's constant, the second term in the equation represents Free Space Loss.

The calculation does not include any additional losses due to atmospheric gasses, rain etc. As satellite EIRP at the beacon frequency is unknown there are 3 values included in Table 5. 50 dBW is equivalent to transponder EIRP as shown in figure 3.1, 9 dBW is a minimal value listed on [28], 30 is given as a middle value of these two.

Table 5 shows that even for the lowest satellite EIRP the C/N is still almost 24 dB which should be enough to measure most of the propagation phenomena

Satellite EIRP [dBW]	9	30	50
Distance to satellite [km]	39690	39690	39690
Free Space Loss [dB]	-210.3	-210.3	-210.3
1/k [dBK-1]	228.6	228.6	228.6
Receiver G/T [dBK]	21.1	21.1	21.1
Received C/N0 [dB]	48.4	69.4	89.4
C/N using 300 Hz RBW [dB]	**23.6**	**44.6**	**64.6**
Received power at antenna output assuming 70% efficency [dBm]	-127.5	-106.5	-86.5
Feed loss [dB]	0.4	0.4	0.4
LNB gain [dB]	59	59	59
Cable and splitter losses [dB]	11.6	11.6	11.6
Received power at SA input [dBm]	**-80**	**-59**	**-39**

Table 5 Link budget calculations

3.4 Meteorological data

Meteorological data were obtained from a nearby meteorological station operated by the Norwegian Meteorological Institute. The data obtained each hour were: Temperature, Atmospheric Air Pressure and Humidity. Precipitation intensity with 1 minute integration time was obtained as well, minimal value that could be measured was 0.1 mm / minute (6 mm/h).

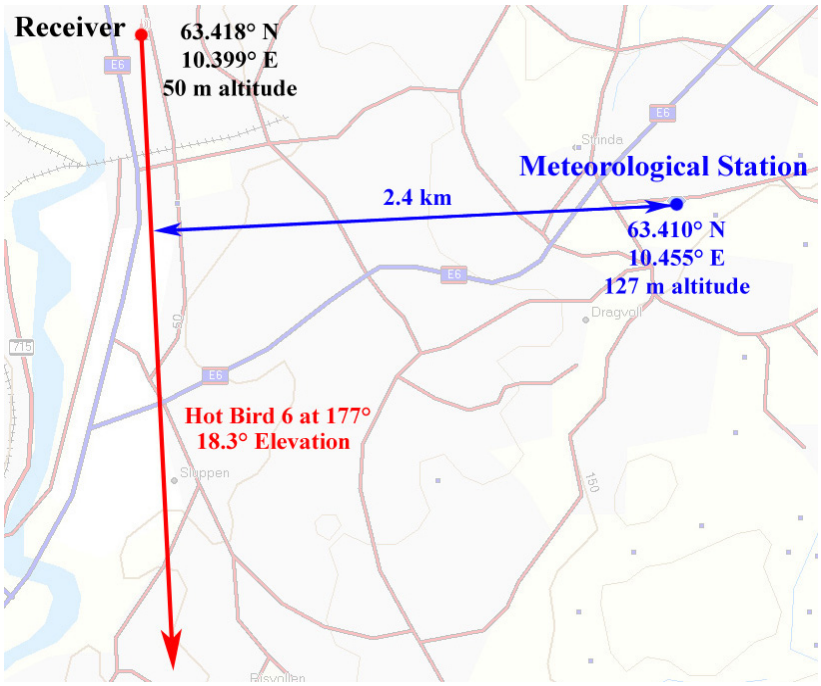

Figure 3.13 Relative location of the receiver and the meteorological station

The Temperature, Pressure and Humidity values were corrected to the receiver altitude using equations for reference standard atmosphere given in [6] for summer atmosphere at high latitudes.

As Figure 3.13 shows the station is located about 3 kms southeast of the receiver and about 2.4 km east from the propagation path. No instantaneous correlation can therefore be expected between rain at the meteorological station and rain at the propagation path. Long term statistics should, however, correlate rather well as shown in [4] on page 166.

Chapter 4

Measured Results and Analysis

In this section the first short-term measurement results are presented and compared with model data. It should be noted that the models used are intended to model periods of 1 month and long while the measurement was done only in 25 days and out of these not all measured data was usable.

Figure 4.1 shows the received spectrum of the Hot Bird 6 beacon. In addition to the main beacon signal there are additional ones with a power level 20 and 28 dB lower. These are 100 Hz away from the main beacon signal. Possible explanations are either that the beacon is modulated with telemetry data or that these are intermodulation or mixing products.

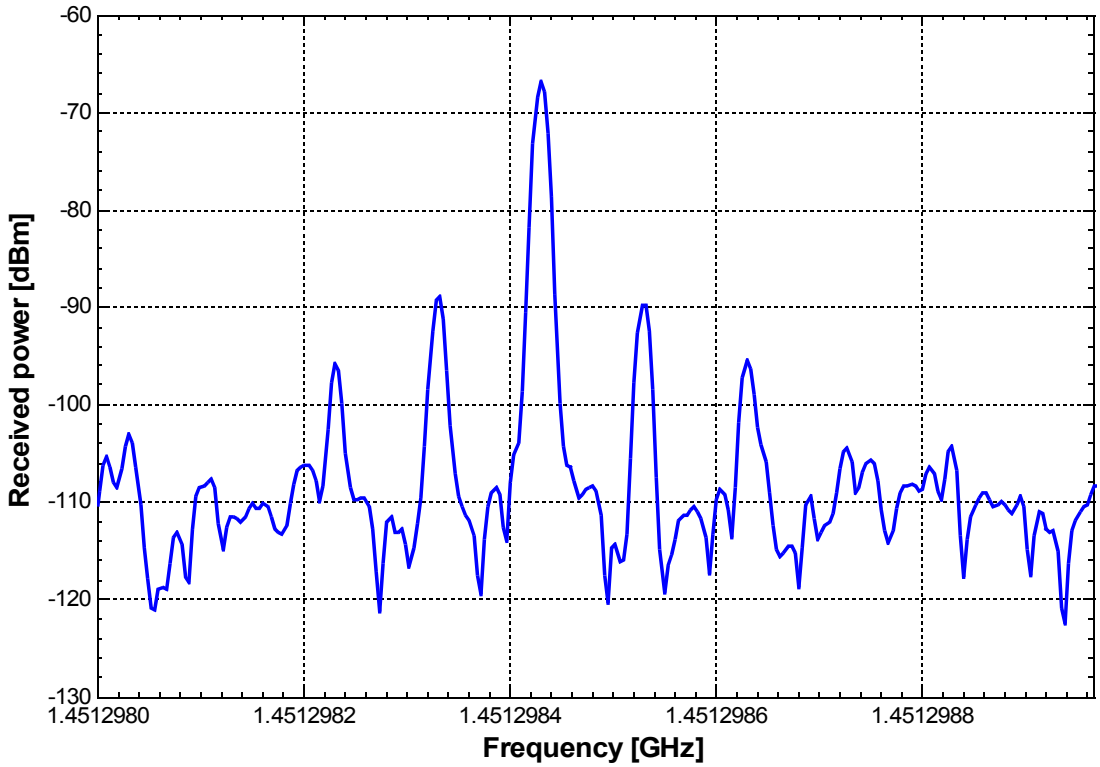

Figure 4.1 Received Hot Bird 6 beacon spectrum at the IF, RBW of the spectrum analyzer is set to 10 Hz.

Received frequency of the beacon moved as much as ±15 kHz over the course of a few days. This might be caused by either satellite beacon instability, LNB LO instability (should be as stable as the reference generator), reference generator instability or spectrum analyzer reference instability

(should be ± 1 ppm according to specification [25]) or even Doppler shift due to slightly changing position of the satellite. Most likely it is a combination of the above. For long term measurement frequency span of 200 kHz and RBW of 300Hz were used to prevent losing track of the beacon while keeping reasonably short sweep times.

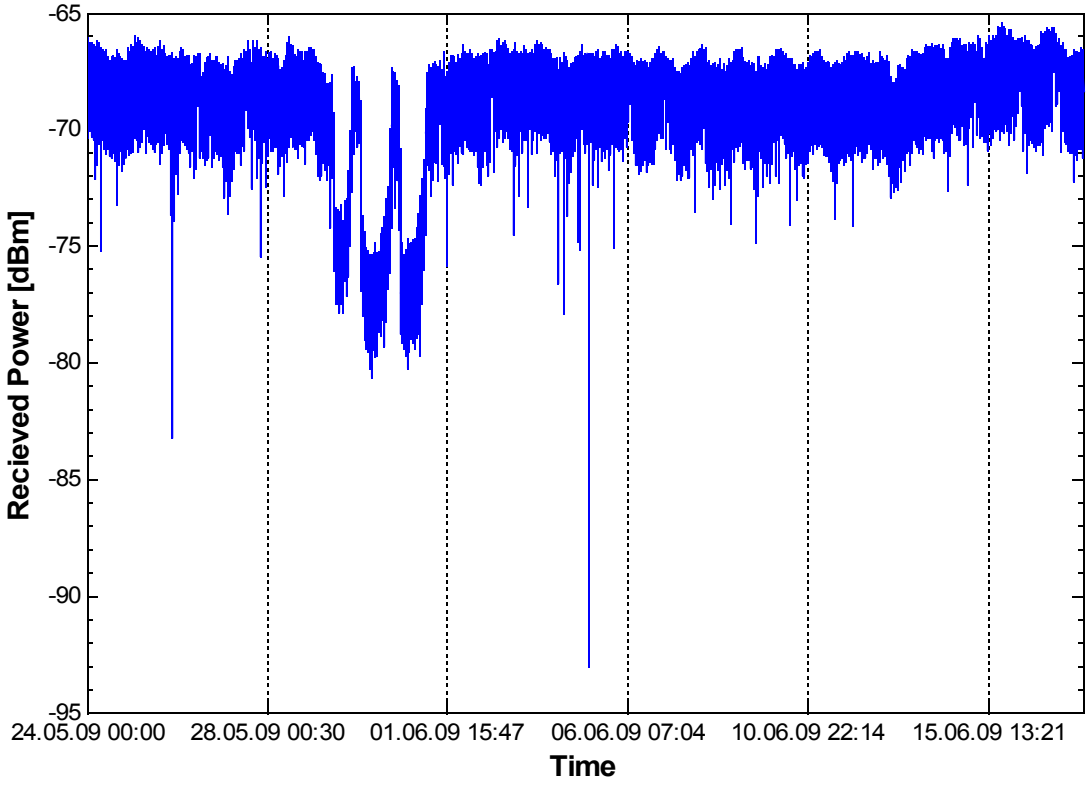

Figure 4.2 Data from 25 days of measurements after subtracting noise data

Figure 4.2 shows 25 full days of measured data, the uneven scale is caused by non-constant time between each value as described in section 3.2.2 Between 29.05. and 01.06 the received power shows 3 significant decreases, two of them starting or ending during the night. The cause is most likely satellite-related, but it is impossible to determine it without knowledge of satellite status.

Another event visible on both Figure 4.2 and Figures 4.3 and 4.4 is the slow increase of received power from 13.06. onwards. As for the previous event it is not possible to determine the cause without satellite status data. A possible cause is a satellite position or orientation correction. The very small decrease in daily average of received power (visible on Figure 4.4) since the start of measurement seems to confirm this.

Finally the data displays diurnal variation, this is most clearly visible on Figure 4.4. This effect similar to the one illustrated on page 182 of [4], is caused by variances in satellite position. Gravitational forces from Moon and Sun move a geostationary satellite slowly out of position increasing its inclination to a non-zero one. Since this effect is constant over time corrections are made only when the position derives a certain amount, leading to the measured variation when

uncorrected.

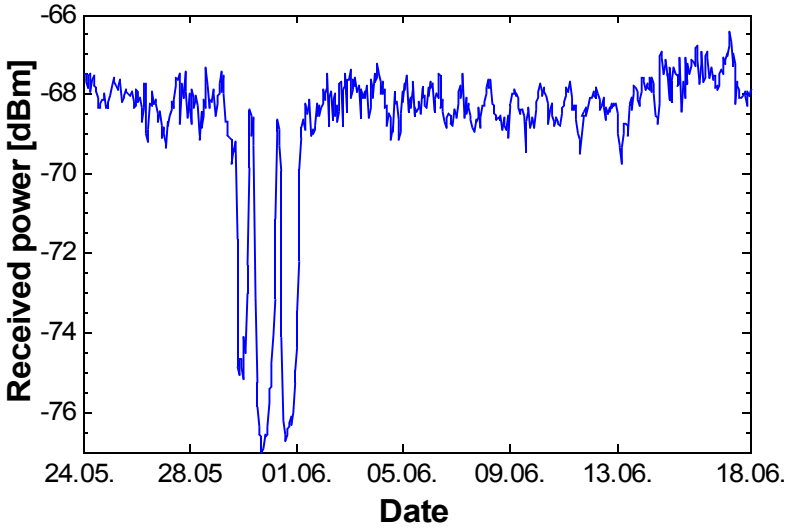

Figure 4.3 Hourly averaged data for 25 days of measurements

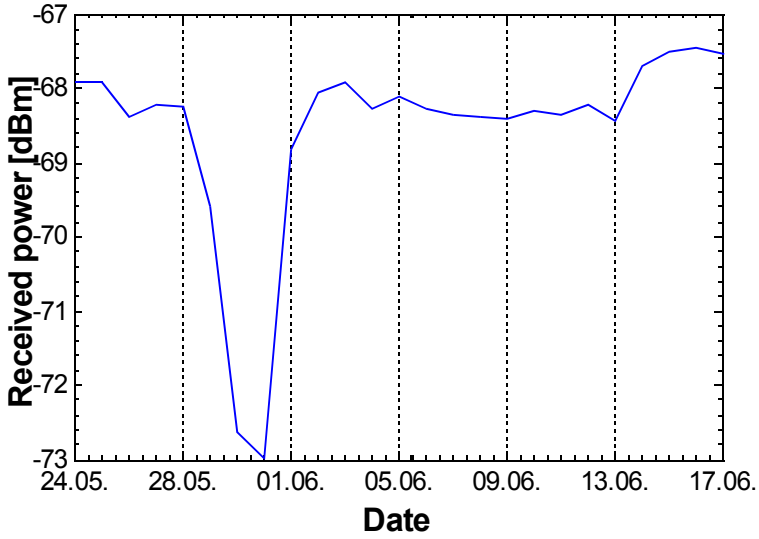

Figure 4.4 Daily averaged data for 25 days of measurements

In the following sections the measured data and meteorological data for same period are analyzed to investigate the effect of the different propagation phenomena. The data between 28.05 – 02.06. are removed from all calculations. Data after 13.06 are removed from all but scintillation calculations as these are examined using short-time data which should not be significantly affected by this slow change.

4.1 Attenuation Due to Atmospheric Gases

Since the satellite EIRP is unknown, it is impossible to try to asses attenuation by atmospheric gases from the received power. The meteorological data for the period does, however, allow to use the simplified model as outlined in Appendix A2 to calculate it. This data can then be subtracted from the measured data when investigating other long-term phenomena.

The meteorological data provided by Norwegian Meteorological Institute gives temperature, pressure and humidity for each whole hour. As mentioned before they were first adjusted for the small altitude difference between the meteorological station and the receiver. To make the results comparable with measured hourly averages, the data set was converted into values valid for the middle of each hour by taking average of the two neighboring full hour values. Humidity data was converted into water vapour density using equations given in Appendix A4.

Attenuation due to atmospheric gases was then calculated using equations from Appendix A2. The results shown in Figure 4.5 show surprisingly large variations for such a short period of time reaching almost 0.4 dB in difference.

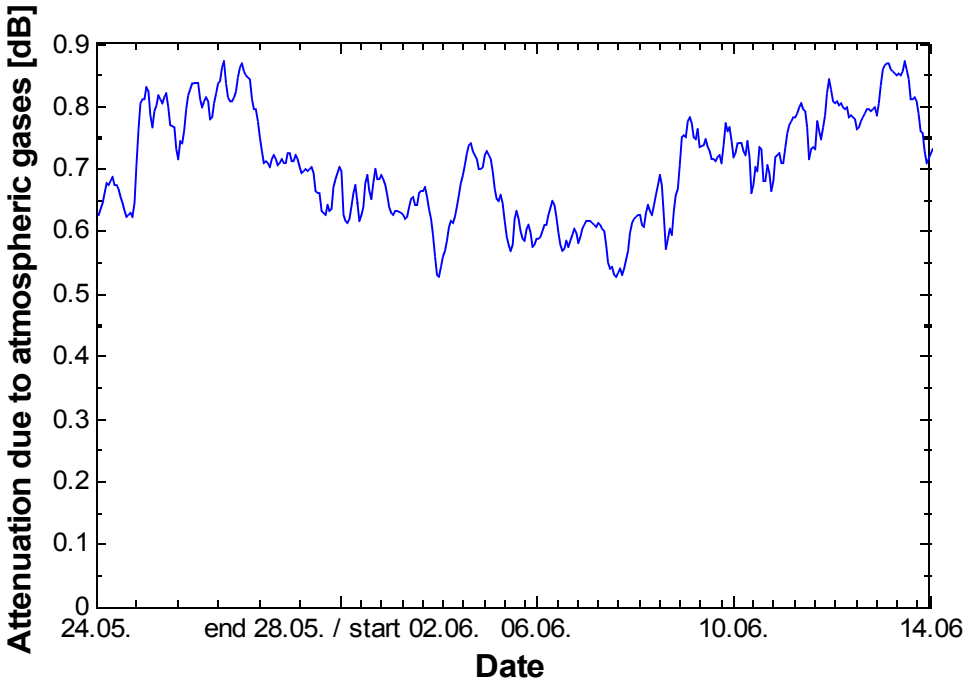

Figure 4.5 Attenuation due to atmospheric gases calculated using local meteorological data.

4.2 Scintillation

To asses the effect of scintillation alone, minute average of the received power was subtracted from the measured data. This minute average component should include most of the effects caused by atmospheric gases, precipitation, clouds and fog, as well as differences due to the movement of the satellite.

Histogram of the resulting data is shown in Figure 4.6, the calculated mean of the data is 0.027 dB. This seems to follow the assumption of scintillation being normally distributed with zero mean.

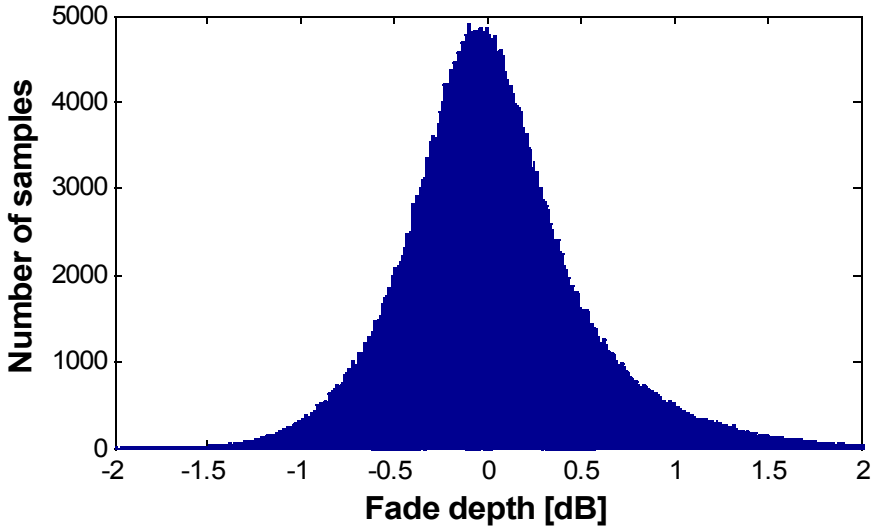

Figure 4.6 Histogram of the measured scintillation data

For comparison, expected scintillation fade dept exceeded between 50% and 0.01% of time was calculated using both the ITU-R model given in Appendix A4 as well as the van de Kamp model which uses modified reference scintillation deviation as calculated by equations (9) and (9a). Temperature, pressure and humidity data was averaged from the meteorological data for the measurement days. Yearly average water content of heavy clouds used in the van de Kamp model was taken from the map in [12].

This comparison shown in Figure 4.7 displays much higher measured fade depths than predicted by both models. As previous measurements [2] have mostly shown that the ITU-R model tends to overpredict, this significant difference seems to point to some flaws within the measurement or the measurement system. One possible source of error is that the minute averaging does not completely remove the effect of variations in rain intensity that are faster than 1 minute. While measurements in Kjeller [2] did not show this problem it should be noted that Kjeller has a more inland climate and hence rain that tends to cover a larger area and change slowly, while Trondheim experiences short swells of more intensive rain.

Another factor which might be heavily contributing is the accuracy of the spectrum analyzer used for measurement. According to specification it should only have about ± 1.5 dB absolute amplitude accuracy. Relative amplitude accuracy over 1 minute which is used here is, however, unknown.

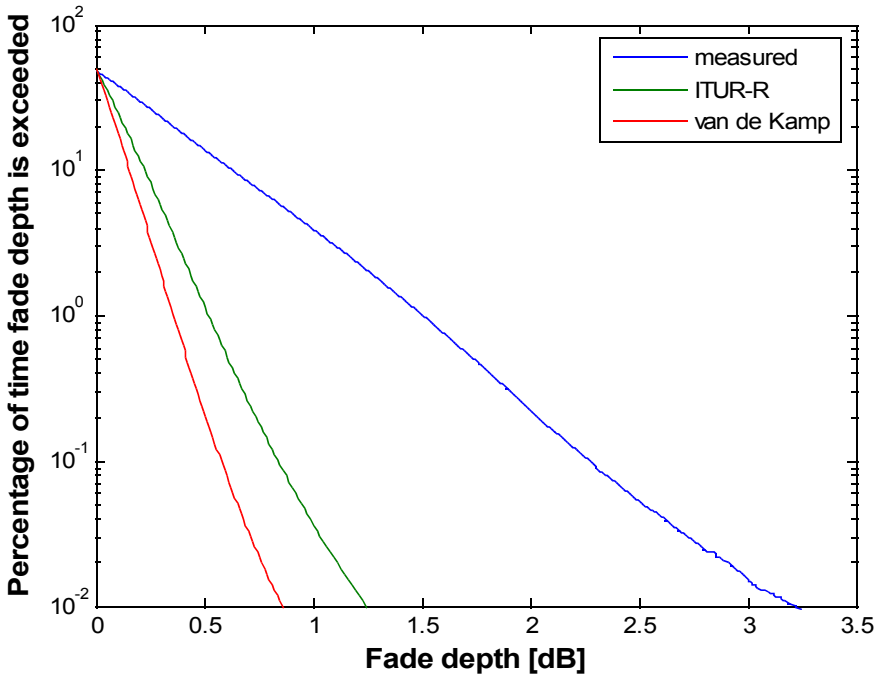

Figure 4.7 Measured scintillation fade depth in comparison with models

4.3 Total Attenuation Due to Clouds, Rain and Scintillation

Separating attenuation only due to rain and clouds/fog from the measured data is virtually impossible. These phenomena were therefore assessed together with scintillation by using the relation given in chapter 2.5 of [11]:

$$A_T(p) = A_G(p) + \sqrt{((A_R(p) + A_C(p))^2 + A_S^2(p))} \qquad (24)$$

where:

$A_G(p)$ - attenuation due to atmospheric gases for a given probability (p)

$A_R(p)$ - attenuation due to rain a given probability (p)

$A_C(p)$ - attenuation due to clouds for a given probability (p)

$A_S(p)$ - attenuation due to tropospheric scintillation for a given probability (p)

The equation should be valid for a probability between 0.001% and 50%. For a probability less than 1 %, $A_C(p)$ and $A_G(p)$ should be equal to $A_C(1\%)$ respective $A_G(1\%)$.

In our case attenuation due to atmospheric gases as calculated in section 4.1 was subtracted directly from the measured data. Cloud attenuation was calculated using the ITU-R model [20], average values for total columnar content of liquid water from a 40 year ERA40 dataset by ECMWF were used in these calculations due to insufficient local data. Scintillation, calculated using the ITU-R model given in Appendix A4, used same measured meteorological data as in section 4.2, except only for 17 days. Rain attenuation was calculated using ITU-R model given in Appendix A5 and used rain intensity data collected at the meteorological station. The measured rain intensity exceeded during 0.01% of the time was 18 mm/hour, rain height used for the calculation was also from the ERA40 dataset.

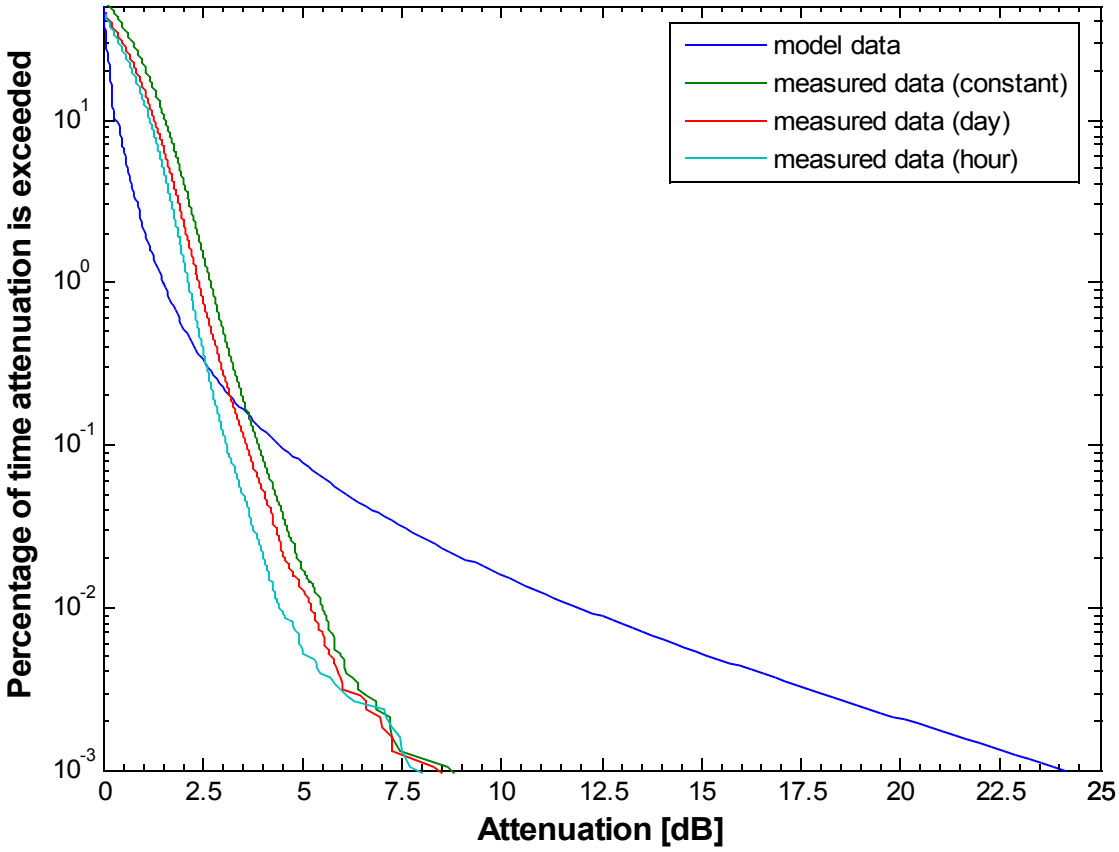

Figure 4.8 Model data for combined cloud, scintillation and rain attenuation in comparison with measured data

When analyzing the measured data, the most difficult part is the identification of a clear sky reference level. This is further augmented by the diurnal variations of the signal level which were observed. For this reason 3 different approaches were chosen for comparison: subtracting hourly mean value, subtracting daily mean value and subtracting mean value of a day with no clouds and precipitation (24.05). All these were calculated from the dataset with gas attenuation already subtracted. The comparison of the measured data with the modeled ones is given in Figure 4.8.

The higher measured attenuation exceeded in 50%-0.5% of time can be possibly explained by the amplitude measurement problems mentioned in section 4.2. The much lower measured attenuation for smaller percentages must have different causes. The relatively low sampling rate during the measurement (about 1 sample every 4 seconds) might be a contributing factor. Since this attenuation should be caused primarily by rain it is possible that the ITU-R rain model does not reflect the local character of powerful rain showers in the Trondheim area.

Chapter 5

Conclusion and Recommendations for Future Work

In this report a brief description of the main phenomena affecting radiowave propagation at earth-satellite links in high latitude regions was given. Models for long-term modeling of the effects of these phenomena were presented.

To confirm the accuracy of these models for high-latitude locations and low elevation angles a simple measurement system was designed. When designing the system focus was put on low cost, simplicity and availability of components. Some new components had to be locally designed and manufactured. Afterwards these new components were measured (when possible) and found to fulfill the required criteria. The system was assembled and the overall system sensitivity checked through G/T measurement. After the system started operation, 25 days of measured data were collected and compared with chosen models. Local meteorological data was used in these models where applicable.

Analysis of the results showed the need for several improvements of the measurement system. The unavailability of satellite status data emerged as a hindrance to clearly asses unusual events and remove their influence on the measurement. The spectrum analyzer used was identified as a possible source of errors due to its relatively low amplitude accuracy of only ± 1.5 dB, midrange desktop spectrum analyzers achieve accuracy of about ± 0.2 dB so a different spectrum analyzer should be used as soon as possible for comparison and eventual replacement. Optionally a power meter with a narrow band filter might be used, but this creates new challenges in the steepness and bandwidth of the filter as well as in the slight frequency drift of the received signal. Sampling rate of the system should also be increased for future measurements.

The rain measurement seem to suggest possible shortcomings of the ITU-R theoretical model so a long term measurement of rain attenuation should be performed in the future. In relation to this, it is advisable to attach a local meteorological station to the receiver providing on-site meteorological data as the station currently used is located some distance away. Data from these two stations can also be compared to identify different rain events.

Most of the components were purchased in pairs so that a second station using a second antenna of same type which is available on NTNU could be put into operation in the future. It can then be placed either on a different location in the country or used for local diversity measurements.

Finally the feed assembly on the antenna could be improved to operate over a wider frequency range by designing a multi-section waveguide converter and possibly ever further by purchasing LNBs for different frequency bands. Motors for antenna tracking could also be added to the antenna to allow easier measurement, even when using non-geostationary satellites, increasing the number of possible elevation angles and locations that can be investigated.

Appendix

A1 Line-by-line calculation of gaseous attenuation

In this section the procedure for calculation of gaseous attenuation at satellite links operating on frequencies up to 1THz according to [5] is described.

A1.1 Specific Attenuation

Specific attenuation is summation of parts of all individual resonance lines for oxygen and water vapour as well as additional factor for non-resonant Debye spectrum of oxygen below 10GHz, pressure-induced nitrogen attenuation above 100GHz and wet continuum to account for excess water vapour found experimentally.

Specific gaseous attenuation is given by:

$$\gamma = \gamma_0 + \gamma_w = 0.1820\ f\ imag[N(f)] \qquad \text{dB/Km} \qquad \text{(A.1)}$$

where γ_0 and γ_w are specific attenuations due to dry air and water vapour in dB/km , f is frequency in GHz and `imag[N(f)]` is the imaginary part of complex refractivity:

$$imag[N(f)] = \sum_i S_i\ F_i + imag[N_D(f)] \qquad \text{(A.2)}$$

S_i is the strength of the i-th line, F_i is the line shape factor and N_d is the dry continuum due to pressure-induced nitrogen absorption and the Debye spectrum.

The line strength is given by:

$$S_i = a_1 x\, 10^{-7}\, p\, \theta^3 \exp[a_2(1-\theta)] \qquad \text{for oxygen} \qquad \text{(A.3a)}$$

$$S_i = b_1 x\, 10^{-7}\, e\, \theta^3 \exp[b_2(1-\theta)] \qquad \text{for water vapour} \qquad \text{(A.3b)}$$

where:

p – dry air pressure (hPa)

e – water vapour partial pressure in hPa (total barometric pressure P = p+e), can also be obtained from water-vapour density ρ using expression

$$e = \rho T / 216.7 \qquad \text{(A.4)}$$

θ = 300/T
T - temperature (K)

The coefficients a_1,a_2 and b_1,b_2 can be found in [4]

The line-shape factor is given by:

$$F_i = \frac{f}{f_i}\left[\frac{\Delta f - \delta(f_i - f)}{(f_i - f)^2 + \delta f^2} + \frac{\Delta f - \delta(f_i + f)}{(f_i + f)^2 + \Delta f^2}\right] \qquad \text{(A.5)}$$

where f_i is the line frequency and Δf is the width of the line.

$$\Delta f = a_3 x\, 10^{-4}\, p\, \theta^{0.8-a_4} + 1.1e^{\theta} \quad \text{for oxygen} \quad \text{(A.6a)}$$

$$\Delta f = b_3 x 10^{-4} (p\ \theta^{b_4} + b_5\ e\ \theta^{b_6}) \quad \text{for water vapour} \quad \text{(A.6b)}$$

The line width Δf is modified by to account for Doppler broadening:

for oxygen
$$\Delta f = \sqrt{\Delta f^2 + 2.25\text{x}10^{-6}} \quad \text{(A.7a)}$$

for water vapour:
$$\Delta f = 0.535\Delta\text{f} + \sqrt{0.217\Delta\text{f}^2 + \frac{2.1316\text{x}10^{-12}\ f_i^{\ 2}}{\theta}} \quad \text{(A.7b)}$$

δ is a correction factor which arises due to interference effects in oxygen lines:

$$\delta = (a_5 + a_{6\theta})\, x10^{-4} (p+e)\theta^{0.8}$$

for oxygen (A.8a)

for water vapour
$$\delta = 0 \quad \text{(A.8b)}$$

Coefficients can be found in [4].

The dry air continuum arises from the non-resonant Debye spectrum of oxygen below 10GHz and a pressure-induced nitrogen attenuation above 100GHz.

$$imag[N_D(f)] = f\ p\ \theta^2 [\frac{6.14\text{x}10^{-5}}{d\,[1+(\frac{f}{d})^{\ 2}]} + \frac{1.4\text{x}10^{-12}\ p\theta^{1.5}}{1+1.9\text{x}10^{-5} f^{1.5}}] \quad \text{(A.9)}$$

where d is the width parameter for the Debye spectrum

$$d = 5.6\text{x}10^{-4}\ p\ \theta^{0.8} \quad \text{(A.10)}$$

A1.2 Slant Path Attenuation

Accurate determination of path attenuation through the atmosphere is done by dividing atmosphere into a large number of horizontal layers of equal pressure, temperature and humidity and calculating specific absorption for each of them using the method described in section 1.2. If locally measured profiles are not available reference standard atmospheres from Recommendation ITU-R P835 [18] can be used. The path length also takes ray bending on the edge of the different layers into account.

Total attenuation is then:

$$A_{gas} = \sum_{n=1}^{k} a_n \gamma_n \ \ dB \quad \text{(A.11)}$$

where γ_n is the specific attenuation calculated using (A.1).

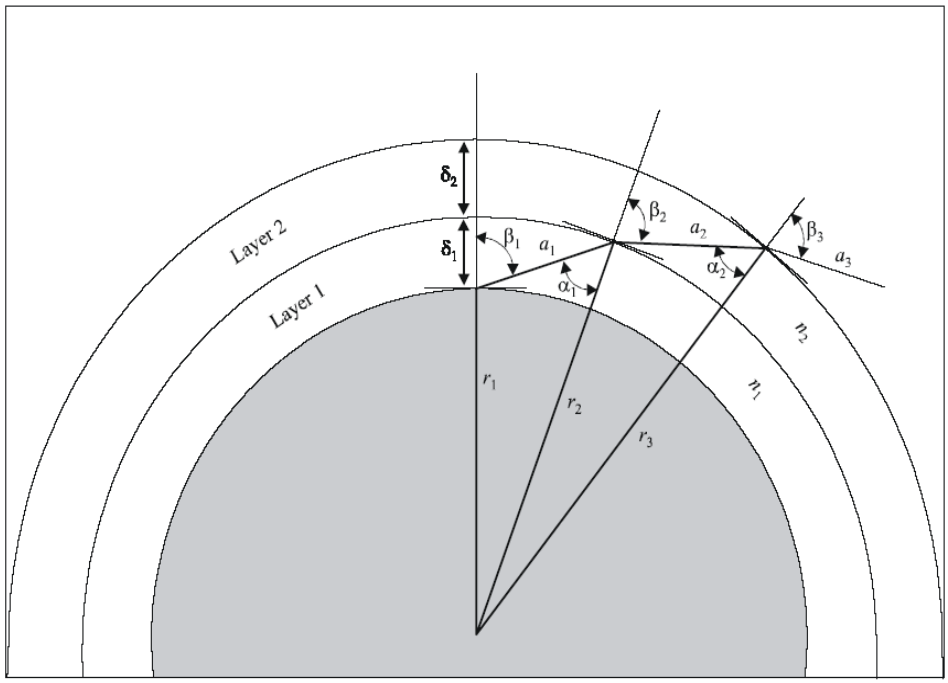

Figure A1 Total path through different layers of atmosphere [5]

Using Figure A1 path length through layer n with thickness δ and refractive index n_n is found. α_n and β_n are the entry and exit incidence angles. R_n are the radii from the centre of the Earth to the beginning of the layer n. a_n can then be expressed as:

$$a_n = -r_n \cos\beta_n + \frac{1}{2}\sqrt{4r_n^2\cos^2\beta_n + 8r_n\delta_n + 4\delta_n^2} \tag{A.12}$$

β_1 is the incidence angle at the ground station and β_{n+1} can be calculated using Snell's law:

$$\beta_{n+1} = \arcsin\left(\frac{n_n}{n_n+1}\sin\alpha_n\right) \tag{A.13}$$

where α_n:

$$\alpha_n = \pi - \arccos\left(\frac{-a_n^2 - 2r_n\delta_n - \delta_n^2}{2a_n r_n + 2a_n\delta_n}\right) \tag{A.14}$$

To ensure accurate estimate of the path attenuation, the thickness of the layers should increase exponentially from 10cm at the lowest layer (ground level) to 1km at an altitude of 100km according to:

$$\delta_i = 0.0001\exp\left(\frac{i-1}{100}\right) \quad km \tag{A.15}$$

for substantial accuracy the integration should be performed at least up to 30km.

A2 Approximate estimation of gaseous attenuation

This section contains simplified algorithms for quick, approximate estimation of gaseous attenuation for frequencies under 54 GHz using surface temperature, pressure and water vapour density as shown in [5].

A2.1 Specific attenuation

For dry air:

$$\gamma_o = [\frac{7.2 r_t^{2.8}}{f^2 + 0.34 r_p^2 r_t^{1.6}} + \frac{0.62 \xi_3}{(54 - f)^{1.16 \xi_1} + 0.83 \xi_2}] f^2 r_p^2 x 10^{-3} \quad dB/km \tag{A.16}$$

with:

$$\xi_1 = \varphi(r_p, r_t, 0.0717, -1.8132, 0.0156, -1.6515) \tag{A.17}$$

$$\xi_2 = \varphi(r_p, r_t, 0.5146, -4.6368, -0.1921, -5.7416) \tag{A.18}$$

$$\xi_3 = \varphi(r_p, r_t, 0.3414, -6.5851, 0.2130, -8.5854) \tag{A.19}$$

$$\varphi(r_p, r_t, a, b, c, d) = r_p^a r_t^b \exp[c(1 - r_p) + d(1 - r_t)] \tag{A.20}$$

where:

f – frequency (GHz)
r_p – p/1013
r_t – 288(273+t)
p – pressure (hPa)
t – temperature (°C)

For water vapour:

$$\gamma_w = F f^2 r_t^{2.5} \rho x 10^{-4} \quad dB/km \tag{A.21}$$

$$F = \frac{3.98 \eta_1 \exp[2.23(1 - r_t)]}{(f - 22.235)^2 + 9.42 \eta_1^2} g(f, 22) + \frac{11.96 \eta_1 \exp[0.7(1 - r_t)]}{(f - 183.31)^2 + 11.14 \eta_1^2} + \frac{0.081 \eta_1 \exp[6.44(1 - r_t)]}{(f - 321.226)^2 + 6.29 \eta_1^2}$$

$$+ \frac{3.66 \eta_1 \exp[1.6(1 - r_t)]}{(f - 325.153)^2 + 9.22 \eta_1^2} + \frac{25.37 \eta_1 \exp[1.09(1 - r_t)]}{(f - 380)^2} + \frac{17.4 \eta_1 \exp[1.46(1 - r_t)]}{(f - 448)^2}$$

$$+ \frac{844.6 \eta_1 \exp[0.17(1 - r_t)]}{(f - 557)^2} g(f, 557) + \frac{290 \eta_1 \exp[0.41(1 - r_t)]}{(f - 752)^2} g(f, 752)$$

$$+ \frac{8.3328 \text{x} 10^{-4 \eta_2} \exp[0.99(1 - r_t)]}{(f - 1780)^2} g(f, 1780) \tag{A.22}$$

with:

$$\eta_1 = 0.955 r_p r_t^{0.68} + 0.006 \rho \tag{A.23}$$

$$\eta_2 = 0.735 r_p r_t^{0.5} + 0.0353 r_t^4 \rho \tag{A.24}$$

$$g(f, f_i) = 1 + \left(\frac{f - f_i}{f + f_i}\right)^2 \quad \text{(A.25)}$$

where ρ is the water vapour density (g/m^3).

A2.2 Slant path Attenuation

Structure of atmosphere is approximated by a single layer for oxygen as well as one for water vapour.

The equivalent height for dry air is:

$$h_o = \frac{6.1}{1 + 0.17 r_p^{-1.1}}(1 + t_1 + t_2 + t_3) \quad \text{(A.26)}$$

where:

$$t_1 = \frac{4.64}{1 + 0.066 r_p^{-2.3}} \exp\left[-\left(\frac{f - 59.7}{2.87 + 12.4\exp(-7.9 r_p)}\right)^2\right] \quad \text{(A.27)}$$

$$t_2 = \frac{0.14\exp(2.12 r_p)}{(f - 118.75)^2 + 0.031\exp(2.2 r_p)} \quad \text{(A.28)}$$

$$t_3 = \frac{0.0114}{1 + 0.14 r_p^{-2.6}} f \frac{-0.0247 + 0.0001\text{f} + 1.61\text{x}10^{-6} f^2}{1 - 0.0169\text{f} + 4.1\text{x}10^{-5} f^2 + 3.2\text{x}10^{-7} f^3} \quad \text{(A.29)}$$

with the constraint that:

$$h_o \le 10.7 r_p^{0.3} \quad \text{(A.30)}$$

Equivalent height for water vapour:

$$h_w = 1.66\left(1 + \frac{1.39\sigma_w}{(f - 22.235)^2 + 2.56\sigma_w} + \frac{3.37\sigma_w}{(f - 183.31)^2 + 4.69\sigma_w} + \frac{1.58\sigma_w}{(f - 325.1)^2 + 2.89\sigma_w}\right) \quad \text{(A.31)}$$

$$\sigma_w = \frac{1.013}{1 + \exp[-8.6(r_p - 0.57)]} \quad \text{(A.32)}$$

Path attenuation for earth-space path with an elevation angle φ between 5° and 90° can then be calculated as:

$$A = \frac{A_o + A_w}{\sin\varphi} \ \ dB \quad \text{(A.33)}$$

where $A_o = h_o \gamma_o$ $A_w = h_w \gamma_w$

Alternatively in case integrated water vapour content along the path is known, alternative method may be used for total water vapour attenuation, estimating it as:

$$A_w(f,\theta,P)=\frac{0.0173\mathrm{V}_t(P)}{sin\theta}\frac{\gamma_w(f,p_{ref},\rho_{v,ref},t_{ref})}{\gamma_w(f_{ref},p_{ref},\rho_{v,ref},t_{ref})}\ dB \qquad (A.34)$$

where:

f- frequency (GHz)
θ- elevation angle (>5°)
f_{ref}- 20.6 (Ghz)
p_{ref}-780 (hPa)

$$\rho_{v,ref}=\frac{V(P)}{4}\ (g/m^3)$$

$$t_{ref}=14\ln(\frac{0.22\,V_t(P)}{4})+3\ (^\circ C)$$

$V_t(P)$ – integrated water vapour content at the required percentage of time
$\gamma_w(f,p,\rho,t)$ - specific attenuation as a function of frequency, pressure, water-vapour density and temperature calculated from (A.21).

A3 Estimation of Apparent Elevation Angle

According to [7] the apparent elevation angle θ (degrees) is given by:

$$\theta=\theta_0+\tau_s(h,\theta_0) \qquad (A.35)$$

the function τ_s (h, θ_0) (degrees) can be approximated by:

$$\tau_s(h,\theta_0)=1/[\,1.728+0.541\,\theta_0+0.03723\,\theta_0^2+h(0.1815+0.06272\,\theta_0+0.01380\,\theta_0^2)+h^2(0.001727+0.008288\,\theta_0)\,] \qquad (A.36)$$

A4 Calculation of Monthly and Long-Term Statistics of Amplitude Scintillations

Given below is a general method for predicting cumulative distribution as outlined in [11].

Required parameters:

t – average surface temperature (°C) at the site for a period of one month or longer

H – average surface relative humidity (%) for a period of one month or longer

f – frequency (Ghz) between 4GHz and 20 Ghz

θ – path elevation angle equal or higher than 4°

D – antenna diameter for the earth-station antenna

η – antenna efficiency

Step1: Calculate water vapour pressure

$$e = \frac{H\, e_s}{100} \quad hPa \tag{A.37}$$

with:

$$e_s = a \exp\left(\frac{bt}{t+c}\right) \quad hPa \tag{A.38}$$

H – relative humidity (%)

e_s – saturation vapour pressure at given temperature

a = 6.1121 for water, 6.1115 for ice

b = 17.502 for water, 22.452 for ice

c = 240.97 for water, 272.55 for ice

Values for water are valid in between -20° and +50°, for ice between -50°C and 0°.

Vapour pressure is related to vapour density ρ by:

$$e = \frac{\rho T}{216.7} \quad hPa \tag{A.39}$$

Step2: Compute wet term of refractivity N_{wet}

$$N_{wet} = 3.732\text{x}10^5 \frac{e}{T^2} \tag{A.40}$$

here T is absolute temperature in Kelvin.

Step3: Calculate the standard deviation of the signal amplitude $\sigma_{ref,}$ to be used as reference:

$$\sigma_{ref} = 3.6\, x10^{-3} + 10^{-4}\, x\, N_{wet} \quad dB \tag{A.41}$$

Step4: Calculate the effective path length L according to:

$$L = \frac{2\text{h}_L}{\sqrt{sin\theta^2 + 2.35\text{x}10^{-4}} + sin\theta} \quad m \tag{A.42}$$

where h_L is the height of the turbulent layer; assumed as h_L=1000m

Step5: Estimate the effective antenna diameter, from geometrical diameter and antenna efficiency η:

$$D_{eff} = \sqrt{(\eta)}\, D \quad m \tag{A.43}$$

Step6: Calculate the antenna averaging factor from:

$$g(x)=\sqrt{3.86(x^2+1)^{11/12}\sin[\frac{11}{6}\arctan\frac{1}{x}]-7.08\,x^{\frac{5}{6}}} \quad \text{(A.44)}$$

where:

$$x=1.22\,D_{eff}^2(f/L) \quad \text{(A.44a)}$$

note that if x≥7.0 the predicted scintillation fade depth for any time percentage is zero

Step7: Calculate the standard deviation of the signal for the considered period and propagation path

$$\sigma=\sigma_{ref}\,f^{7/15}\frac{g(x)}{(sin\theta)^{1.2}} \quad \text{(A.45)}$$

Step8: Calculate the time percentage factor, a(p) for the time percentage, p, of concern in the range 0.01 <p≤50:

$$a(p)=-0.061(\log_{10}p)^3+0.072(\log_{10}p)^2-1.71\log_{10}p+3.0 \quad \text{(A.46)}$$

Step9: Calculate the the scintillation fade depth for the time percentage p by:

$$A_s(p)=a(p)\sigma \quad dB \quad \text{(A.47)}$$

A5. Calculation of Long-Term Rain Attenuation Statistics from Point Rainfall Rate

In this section method for calculating average year attenuation due to rain as unlined in [11] is given.

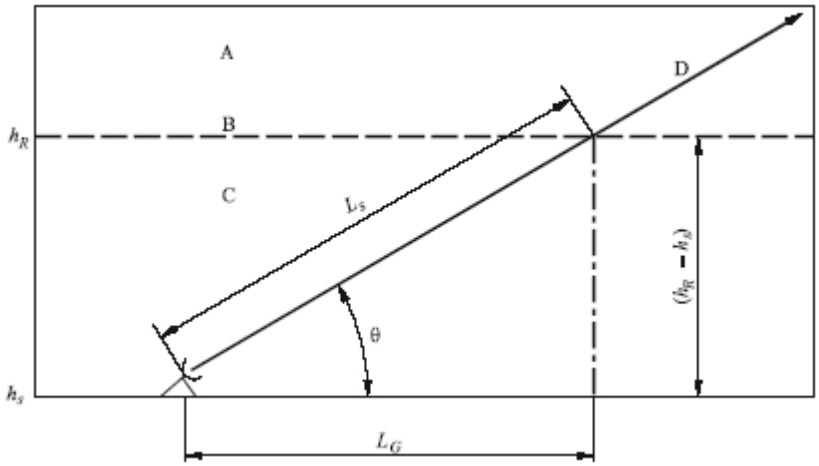

Figure A2 Schematic representation of an Earth-Space path (D), area marked as A contains frozen precipitation, C liquid precipitation and B represents rain height [11]

Step1: Determine the rain height, h_R as given in Recommendation ITU-R P.839:

$$h_R = h_0 + 0.36 \quad km \tag{A.48}$$

h_0 is the mean 0°C height above sea level, this can be obtained locally or from digital maps provided by ITU as was done in this work.

Step2: For elevation angle θ≥5° Compute slant-path length L_s below the rain height from:

$$L_s = \frac{(h_r - h_s)}{sin\theta} \quad km \tag{A.49}$$

for θ≤5° use:

$$L_s = \frac{2(h_r - h_s)}{\left(sin\theta^2 + \frac{2(h_r - h_s)}{R_e}\right)^{(1/2)} + sin\theta} \quad km \tag{A.50}$$

Where h_s is station height above mean sea level in km and R_e is effective earth radius (8500km)

Note that if h_r-h_s less than or equal to zero, the predicted rain attenuation for any time percentage is zero.

Step3: Calculate the horizontal projection, L_G, of the slant-path length from:

$$L_G = L_s \cos\theta \quad km \tag{A.51}$$

Step4: Obtain the rainfall rate, $R_{0.01}$, exceeded for 0.01% of an average year (with a 1 min integration time). This can be calculated from local data or from the rainfall maps given in ITU-R P.837.

Step5: Calculate the specific attenuation, γ_R, using:

$$\gamma_R = k(R_{0.01})^{\alpha} \quad dB/km \tag{A.52}$$

The frequency-dependent coefficients α and k are give in Recommendation ITU-R P.838 [16].

Step6: Calculate the horizontal reduction factor, $r_{0.01}$, for 0.01% of the time:

$$r_{0.01} = \frac{1}{1 + 0.78\sqrt{\frac{L_G \gamma_R}{f}} - 0.38(1 - e^{-2L_G})} \tag{A.53}$$

Step7: Calculate the vertical adjustment factor, $\upsilon_{0.01}$, for 0.01% of the time:

$$\upsilon_{0.01} = \frac{1}{1+\sqrt{\sin\theta}\left(31\left(1-e^{(\theta/(1+\chi))}\right)\frac{\sqrt{L_R\gamma_R}}{f^2}-0.45\right)} \tag{A.54}$$

where:

For $\zeta>\theta$,

$$L_R = \frac{L_G r_{0.01}}{\cos\theta} \quad km \tag{A.55}$$

Else:

$$L_R = \frac{h_R - h_s}{\sin\theta} \quad km \tag{A.56}$$

with ζ calculated as:

$$\zeta = \tan^{-1}\left(\frac{h_R - h_s}{L_G r_{0.01}}\right) \quad degrees \tag{A.57}$$

If $|\varphi|<36°$,

$$\chi = 36 - |\varphi| \quad degrees \tag{A.58}$$

$$\chi = 0 \tag{A.59}$$

Step8: The effective path length is then:

$$L_E = L_R \upsilon_{0.01} \quad km \tag{A.60}$$

Step9: The predicted attenuation exceeded for 0.01% of the average year is obtained from:

$$A_{0.01} = \gamma_R L_E \quad dB \tag{A.61}$$

Step10: The estimated attenuation to be exceeded for other percentages of an average year, in the range 0.001% to 5% is determined from the attenuation to be exceeded for 0.01% of the average year by:

If $p\geq1\%$ or $|\varphi| \geq 36°$:

$$\beta = 0$$

If $p<1\%$ and $|\varphi|< 36°$ and $\theta\geq25°$:

$$\beta = -0.005(|\varphi| - 36)$$

Otherwise:

$$\beta = -0.005(|\varphi| - 36) + 1.8 - 4.25\sin\theta$$

$$A_p = A_{0.01}\left(\frac{p}{0.01}\right)^{-(0.655+0.033\ln(p)-0.045\ln(A_{0.01})-\beta(1-p)\sin\theta)} \quad dB \tag{A.62}$$

A6 Calculation of Long-Term Statistics of Hydrometeor-Induced Cross-Polarization

This section includes the method for calculation of cross-polarization discrimination (XPD) statistics from rain attenuation statistics for the same path as given in [11]. It should be valid between 8 and 35 GHz and for elevation angles less than 60°.

Step1: Calculate the frequency-dependent term:

$$G_f = 30 \log f \tag{A.63}$$

f in GHz

Step2: Calculate the rain attenuation dependent term:

$$G_A = V(f) \log A_p \tag{A.64}$$

where:

$$V(f) = 12.8 \mathrm{f}^{0.19} \quad for\, 8 \le f \le 20 \quad GHz$$
$$V(f) = 22.6 \quad for\, 20 < f \le 35 \quad GHz$$

A_p is rain attenuation (dB) exceeded for the required percentage of time.

Step3: Calculate the polarization improvement factor:

$$G_\tau = -10 \log(1 - 0.484(1 + \cos 4\tau)) \tag{A.65}$$

where τ is tilt angle between linearly polarized electric field vector with respect to the horizontal (45° is used for circular polarization).

Step4: Calculate the elevation angle-dependent term:

$$G_\theta = -40 \log(\cos\theta) \tag{A.66}$$

Step5: Calculate the canting angle dependent term:

$$G_\sigma = 0.0052\sigma^2 \tag{A.67}$$

σ is the effective standard deviation of the raindrop canting angle distribution in degrees, it takes value 0°, 5°,10° and 15° for 1%, 0.1%, 0.01% and 0.001% of the time.

Step6: Calculate rain XPD not exceeded for p% of the time:

$$XPD_{rain} = C_f - C_A + C_\tau + C_\theta + C_\sigma \quad dB \tag{A.68}$$

Step7: Calculate the ice crystal dependent term:

$$C_{ice} = XPD_{rain}\, x\, (0.3 + 0.1 \log p)/2 \quad dB \tag{A.69}$$

Step8: Calculate the XPD not exceed for p% of the time, including ice effects

$$XPD_p = XPD_{rain} - C_{ice} \quad dB \tag{A.70}$$

A7 Antenna Specifications with Original 10 -14 GHz Feed

FIBO GREGORIAN OFFSET ANTENNA 90CM

SPECIFICATIONS

AMBIENT CONDITIONS

- TEMP.LIMITS	- 40 to +60 C
- WIND LOAD SURVIVAL	50 m/s
- WIND LOAD OPERATIONAL	36 m/s
- REL.HUMIDITY	10 - 100 %

MECHANICAL DESIGN

- MAIN REFLECTOR	PRESSED ALUMINIUM
- SUB REFLECTOR	CASTED ALUMINIUM
- FEEDHORN	CASTED ALUMINIUM
- SURFACE TREATMENT	CROMATED /POLYESTER
- ANTENNA OPTICS	TWO REFLECTOR GREGORIAN OFFSET
- MOUNT TYPE	ELEVATION OVER AZIMUTH
- ELEVATION RANGE (WITH TELESCOPE)	0 - 60 (FINE ADJUSTMENT)
- AZIMUTH RANGE	360 (FINEADJUSTMENT +/- 2)
- FEEDADAPTER	C 120 / W 75 (360 ROTATION)

ELECTRICAL SPECIFICATIONS

- EFFECTIVE APERTURE		90 CM (90CM x 99 CM)
- OPERATING FREQUENCY		RECIEVE : 10.70 - 12.75 GHz
		TRANSMIT : 14.00 - 14.50 Ghz
- GAIN	11,70 Ghz	RECIEVE : 40,0 dB
	14,25 Ghz	TRANSMIT : 42,0 dB
- SIDELOBE ENVELOPE CO-POL		
	2,5 < O < 7	29- 25 Log O
	7 < O < 9,2	+ 8 dB
	9,2 < O < 48	32- 25 Log O
	48 < O < 180	-10 dB
- CROSSPOL.ISOLATION		-35 dB (- 1 dB CONTOUR)
- VSWR		< 1,2
- HALF POWER BEAMWIDTH		1,75
- NOISE TEMP.(20 - 50 ELEVATION)		23,1 K
- EFFICIENCY		82 %
- G/T (NOISE FIG. 1.0 dB, 11,7 Ghz)		19,7 dB/K

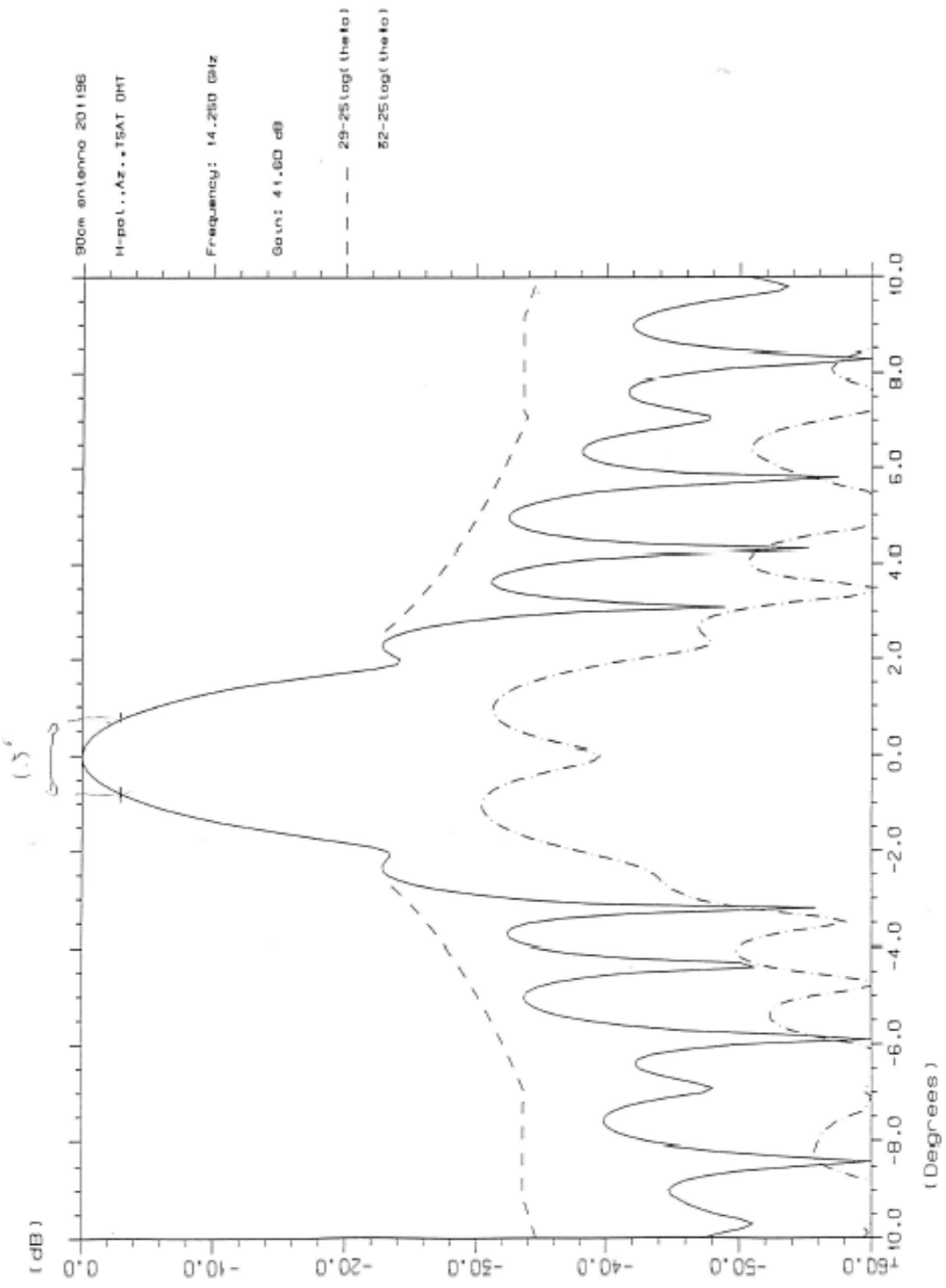
90cm antenna 20198
H-pol.,Az.,ISAT OMT
Frequency: 14.250 GHz
Gain: 41.60 dB
29-25log(theta)
32-25log(theta)
(dB)
0.0
-10.0
-20.0
-30.0
-40.0
-50.0
-60.0
10.0
8.0
6.0
4.0
2.0
0.0
-2.0
-4.0
-6.0
-8.0
-10.0
(Degrees)

A8 20 GHz Feedhorn Blueprint

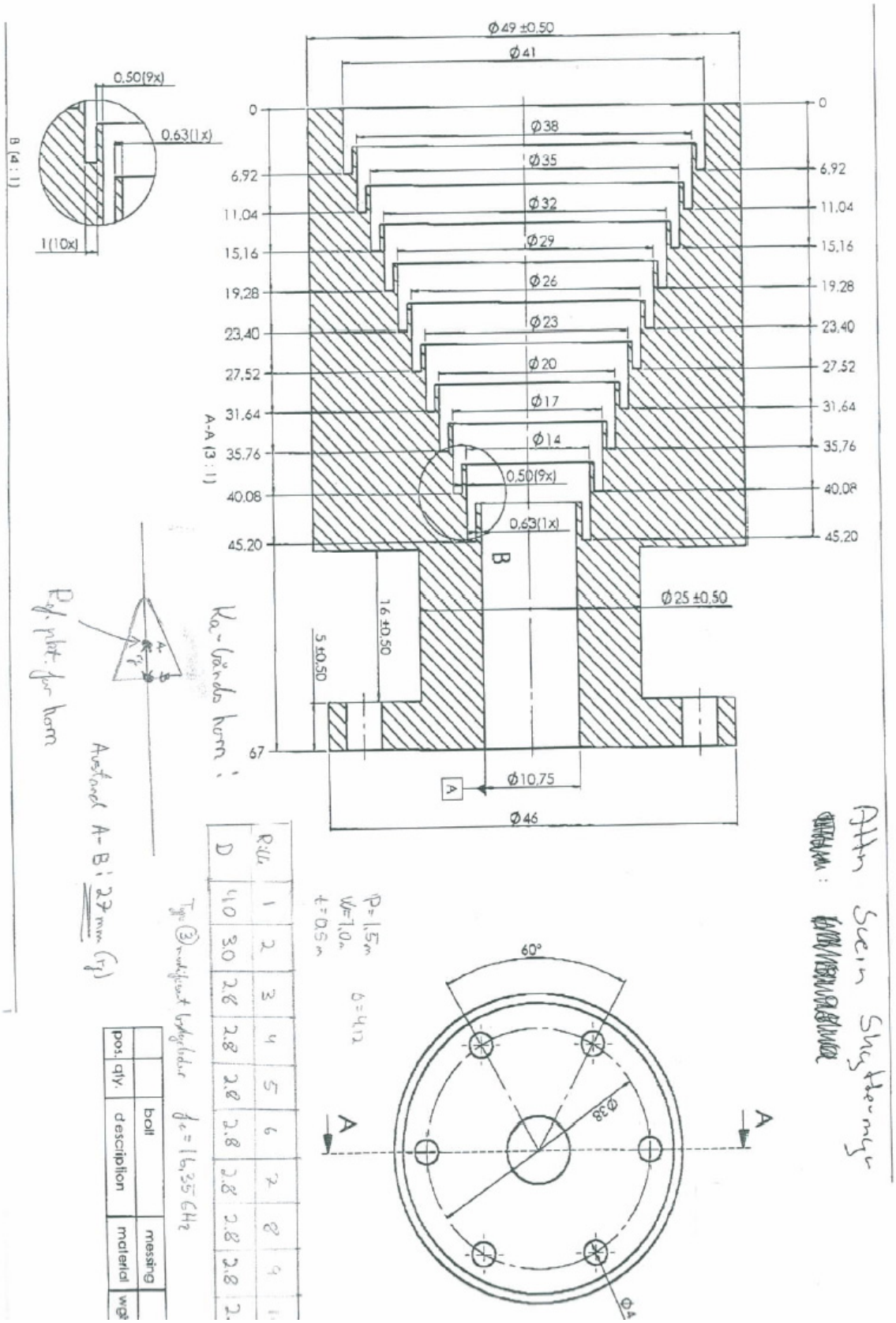

A9 LNB Specifications

Norsat International Inc.

Intelligent Satellite Solutions

30 Years of Excellence

LNB

KA-BAND EXT. REF 9000X

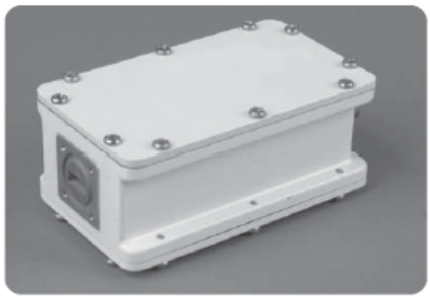

TYPICAL SPECIFICATIONS

Noise figure	1.4 dB
L.O. stability	Phase Locked to External Reference
Phase noise (SSB)	-65 dBc/Hz at 1kHz -75 dBc/Hz at 10kHz -95 dBc/Hz at 100kHz -100 dBc/Hz at 1MHz
Input VSWR	2.2 : 1
Output VSWR	2.0 : 1

Conversion gain	56 dB
Output P1dB	5 dBm
Power requirements	+15 to +24 V supplied through center conductor of IF cable
Current drain	300 mA
Input Waveguide	WR42
Dimensions	122 (L) x 60 (W) x 45 (H) mm (4.8 x 2.4 x 1.8 in)
Weight	400g / 14.1 oz
Ext Ref Frequency	10 MHz (sine-wave), -10 to 0 dBm
Temperature Range	-40°C to +60°C

FREQUENCY BANDS AVAILABLE

Typical service	9000XA	9000XB	9000XC	9000XD (*special order)
Input frequency (GHz)	18.20 to 19.20	19.20 to 20.20	20.20 to 21.20	21.20 to 22.20
L.O. frequency (GHz)	17.25	18.25	19.25	20.25
Output frequency (MHz)	950 to 1950	950 to 1950	950 to 1950	950 to 1950

HOW TO ORDER KA-BAND 9000X

9000XAN

- CONNECTOR.....F - 75 Ohm, N - 50 Ohm
- FREQUENCY.....A - 18.20 - 19.20 GHz, B - 19.20 - 20.20 GHz, C - 20.20 - 21.20 GHz, D - 21.20 - 22.20 GHz
- EXTERNAL REFERENCE
- LNB SERIES #

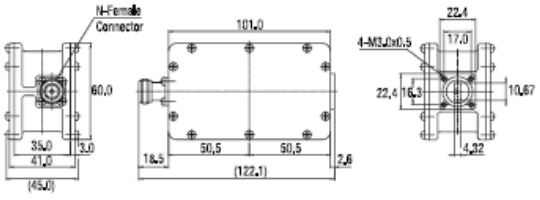

MECHANICAL DIAGRAM

Norsat International Inc.

Americas	Asia	Europe, Middle East & Africa	Online
tel + 1.800.644.4562	tel +1 604.821.2835	tel + 44.1522.730800	info@norsat.com
fax + 1.604.821.2801	fax +1 604.821.2801	fax + 44.1522.730927	www.norsat.com

A10 Circular-Circular Waveguide Convertor Design

In order to connect the feedhorn to the circular-rectangular convertor a custom circular-circular convertor was designed. The feedhorn output has a diameter of 10.75 mm while the standard circular-rectangular convertor from Custom Microwave (CR42S-4547S) has a diameter of 11.549 mm. Due to the difficulties involved in manufacturing of gradual transitions as well as only a narrow bandwidth requirement a simple quarter-wave impedance transformer design was used instead.

A quarter-wave transformer utilizes a section of waveguide with impedance equal to:

$$Z_m = \sqrt{Z_1 Z_2} \tag{A.71}$$

where Z_1 and Z_2 are impedances of the two sections that need to be matched. This section is exactly quarter-wave long at the matched frequency.

Wave Impedance of a circular waveguide at given frequency can be calculated from its cut-off wavelength f_c using:

$$Z_0 = \frac{Z_{fs}}{\sqrt{1-(\frac{f_c}{f_{fs}})}} \tag{A.72}$$

where Z_{fs} is the wave impedance of free space (377 Ω)

f_c for the dominant TE_{11} mode of a circular waveguide is calculated using:

$$f_c = \frac{c}{2\pi\sqrt{\varepsilon_r \mu_r}} \frac{1.841}{R} \tag{A.73}$$

here c is speed of light in vacuum, ε_r and μ_r are relative permittivity and relative permeability of the media inside the waveguide (air in our case).

As written above the length of the section needs to be equal to 1/4 of the wavelength. In case of a waveguide the wavelength inside it is different than wavelength in vacuum. The wavelength inside the section with the new impedance can be calculated using:

$$\lambda_{middle} = \frac{\lambda_{fs}}{\sqrt{1-(\frac{\lambda_{fs}}{\lambda_c})^2}} \tag{A.74}$$

Using these formulas the diameter of middle section needed for matching at 19.701 GHz was calculated to be 11.1 mm. Note that the diameter was rounded to the nearest whole tenth of a millimeter. Length of the section was calculated to be 6.4 mm. See Figure A3 for a simplified drawing.

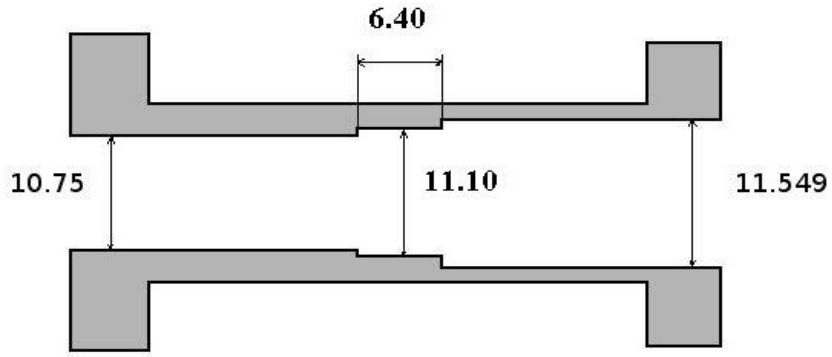

Figure A3 Drawing illustrating the structure of the circular waveguide converter

Waveguide convertor with these dimensions was simulated in Agilent EMDS as well as in CST Microwave electromagnetic simulators. Even using lossy metal models for aluminum the simulation results showed negligible losses on the order of 0.05 dB at the center frequency.

References

[1] O.Gutteberg: ”Low Elevation Propagation in High Latitude Regions”, TF report No. 7/83, Norwegian Telecommunication Research Establishment, 1983

[2] L.E.Bråten: “Comparison of Predicted Scintillation with Data Measured from the 50GHz ITALSAT Beacon in Norway”, Telenor Research and Development, Kjeller, Norway, 2000

[3] Frédéric Lacoste/CNES: ITU-R Propagation Models Software Library, http://logiciels.cnes.fr, February 2006

[4] J.E. Allnutt: “Satellite-to-ground radiowave propagation: Theory, practice and system impact at frequencies above 1 GHz.” Peter Peregrinus Ltd., London,1989

[5] Recommendation ITU-R P.676-7, “Attenuation by atmospheric gases”, P Series, International Telecommunication Union, Geneva, Switzerland, 2007

[6] Recommendation ITU-R P.835-4, “Reference standard atmospheres”, P Series, International Telecommunication Union, Geneva, Switzerland, 2005

[7] Recommendation ITU-R P.834-6, “Effects of tropospheric refraction on radiowave propagation”, P Series, International Telecommunication Union, Geneva, Switzerland, 2007

[8] O. Gutteberg: “Effects of atmosphere on earth-space radio propagation”, Telektronikk 4.92: Satellite communications, 1992

[9] V.I. Tatarski: “Wave Propagation in a Turbulent Medium” (translated by R.A.Silverman). McGraw-Hill, New York, 1961

[10] Hugues Vasseur: “Prediction of Tropospheric Scintillation on Satellite Links from Radiosonde Data”, IEEE Transactions on antennas and propagation, vol. 47. NO. 2, February 1999

[11] Recommendation ITU-R P.618-9, “Propagation data and prediction methods required for the design of Earth-space telecommunication systems”, P Series, International Telecommunication Union, Geneva, Switzerland, 2007

[12] M. M. J. L. van de Kamp, J. K. Tervonen, E.T. Salonen and J.P.V. Poiares Baptista: “Improved Models for Long-Term Prediction of Tropospheric Scintillation on Slant Paths, IEEE Transaction on

antennas and propagation, vol. 47. No.2., February 1999

[13] Y. Karasawa, M. Yamada and J.E. Allnutt: "A new prediction method fro tropospheric scintillation on earth-space paths", IEEE Transactions on antennas and propagation, vol.36, November 1988

[14] M. M. J. L. van de Kamp, J. K. Tervonen, E. T. Salonen, and J. P. V Poiares Baptista: "Scintillation prediction models compared to measurements on a time base of several days", Electron. Lett., vol. 32, 1999

[15] M. M. B. Mohd Yusoff, N. Sengupta, C. Alder, I. A. Glover, P. A. Watson, R. G. Howell and D. L. Bryant: " Evidence for the presence of turbulent attenuation on low-elevation angle earth-spce paths-Part I: Comparison of CCIR recommendation and scintillation observations on a 3.3° path", IEEE Transactions on antennas and propagation, vol. 45, January 1997

[16] W. J. Vogel, G. W. Torrence and J. E. Allnut: "Scintillation fading on a low elevation angle satellite path: Assesing the Austin experiment at 11.2 GHz", 8th Int. Conf. On antennas and Propagation, Edinburg, U.K. Apr. 1993

[17] A. Dissanayake, J. E. Allnutt, F. Haidara: "A Prediction Model that Combines Rain Attenuation and Other Propagation Impairments Along Earth-Satellite Paths", IEEE trans. On antennas and propagation, vol 45. no. 10, october 1997

[18 Recommendation ITU-R P.838-3, "Specific attenuation model for rain for use in prediction methods", P Series, International Telecommunication Union, Geneva, Switzerland, 2005

[19] Recommendation ITU-R P.837-5, "Characteristics of precipitation for propagation modelling", P Series, International Telecommunication Union, Geneva, Switzerland, 2007

[20] Recommendation ITU-R P.840-3, "Attenuation due to clouds and fog", P Series, International Telecommunication Union, Geneva, Switzerland, 1999

[21] Artemis Data Relay Payload Data Book, European Space Agency, Redu, August 2003

[22] UHF satcom page on ka-band reception: http://www.uhf-satcom.com/kaband/
Retrieved 03/2009

[23] Hot Bird 6 Brochure:http://www.eutelsat.com/news/media_library/brochures/hb6_brochure.pdf
Retrieved 04/2009

[24] Too Way brochure: http://www.eutelsat.com/media_library/brochures/tooway.pdf
Retrieved 05/2009

[25] Anritsu MS2721A data sheet, 2006

[26] G. Maran, M. Bousquet: “Satellite Communications Systems”, Figures 5.19-5.20, Fourth Edition, John Wiley & Sons, 2002

[27] R.Flagg, Determination of G/T, http://www.setileague.org/articles/g-t.htm
Retrieved 03/2009

[28] Satellite beacon frequencies page: http://www.satsig.net/eut2beac.htm
Retrieved 03/2009